NOVA
NOVA SCHOOL OF SCIENCE & TECHNOLOGY

DEPARTAMENT OF MATERIALS SCIENCE

JOÃO PEDRO NUNES PIÇARRA
BSc in Micro and Nanotechnology Engineering

Characterization of MEMS Piezoresistive Pressure Sensors

MASTER IN MICRO AND NANOTECHNOLOGY ENGINEERING
NOVA University Lisbon
April, 2025

NOVA SCHOOL OF SCIENCE & TECHNOLOGY

DEPARTAMENT OF MATERIALS SCIENCE

Characterization of MEMS Piezoresistive Pressure Sensors

JOÃO PEDRO NUNES PIÇARRA

BSc in Micro and Nanotechnology Engineering

Adviser: Dr Michael Kraft
Full Professor ESAT - MNS, KU Leuven

Co-advisers: Dr Joana Vaz Pinto
Assistant Professor, NOVA University Lisbon

Examination Committee:

Chair: Dr Pedro Barquinha,
Professor, NOVA University Lisbon

Rapporteurs: Dr Rui Igreja
Professor, NOVA University Lisbon

Adviser: Dr Michael Kraft
Full Professor ESAT - MNS, KU Leuven

Members: Dr Joana Vaz Pinto
Assistant Professor, NOVA University Lisbon
Dr Chen Wang
Postdoctoral researcher ESAT-MNS, KU Leuven

MASTER IN MICRO AND NANOTECHNOLOGY ENGINEERING

NOVA University Lisbon
April, 2025

Characterization of MEMS piezoresistive pressure sensors

Copyright © João Pedro Nunes Piçarra, NOVA School of Science and Technology, NOVA University Lisbon. The NOVA School of Science and Technology and the NOVA University Lisbon have the right, perpetual and without geographical boundaries, to file and publish this dissertation through printed copies reproduced on paper or on digital form, or by any other means known or that may be invented, and to disseminate through scientific repositories and admit its copying and distribution for non-commercial, educational or research purposes, as long as credit is given to the author and editor.

Acknowledgments

First and foremost, I would like to express my deepest gratitude to Professor Michael Kraft for welcoming me into his group, even for a short time. His profound expertise in nanotechnology and the intellectually stimulating environment he cultivates made this project possible.

I am also grateful to my co-advisor, Dr. Chen Wang, for providing challenges and believing in my competences. His help, insightful feedback and constant encouragement during the development of this thesis was invaluable.

I would also like to thank Melexis, specifically Appo van der Wiel, Michiel Gidts and Ben Maes for their collaboration, guidance and the resources provided, which greatly contributed to the successful completion of this work.

A heartfelt thank you goes to my co-advisor in Portugal, Professor Joana Pinto, for always being available, for her constant willingness to help, and for inspiring a genuine love for learning through her teaching. Her passion for knowledge and ability to ignite curiosity in her students is truly admirable.

I would like to express my appreciation to the ESAT staff, whose professionalism ensured that the materials and resources for this thesis were delivered on time and with the highest standards.

A special thanks goes to Donald Raddoux, Rudi Vanlaer and Frederik Daenen, for consistently wire bonding the samples whenever needed, despite an already demanding workload, and for assisting with the printing of the 3D parts. Your help significantly accelerated the progress of this project. I would also like to thank Ruochen for sharing her expertise and helping me grasp important technical concepts.

I am deeply thankful to FCT-NOVA and KU Leuven for making the Erasmus experience possible. My gratitude also goes to my master's coordinator, Hugo Águas, the Erasmus coordinator, Carmo Lança and the staff at the International Relations Division for their dedication and tireless efforts. None of this would have been possible without your work behind the scenes.

A thank you to Gioti, your kindness and belief in me were deeply appreciated. Him and his staff made it possible to adapt quickly in a fast change moment in my life.

To Gelique, thank you for always being there, offering your help and support even when you didn't have to. Your kindness did not go unnoticed.

A very special thanks goes to Bernardo Madeira, whose support went far beyond what was expected. My gratitude to him is infinite.

To Marta, Ana, Fraga, Esmeralda who even though, were far away always stuck with me.

To my friends and colleagues who accompanied me throughout the Erasmus experience - thank you for the laughter, the support, and the unforgettable moments we shared. A special mention to Carolina, András, Amira, and Anujin, who were part of the most memorable adventures in Leuven.

One person I truly couldn't have done this without is Rafael. Your support meant the world to me.

Last but never least, I want to thank my family - my parents, sister, grandparents, cousins and uncle - for standing by me through thick and thin, with unwavering love, patience, and strength. This journey was only possible because of you.

“Sabemos muito mais do que julgamos,
podemos muito mais do que imaginamos.” (Saramago, José).

ABSTRACT

MEMS (Microelectromechanical Systems) piezoresistive pressure sensors are widely used in industries such as automotive, biomedical, and industrial automation, where high sensitivity, compactness, and low power consumption are essential. This dissertation focuses on the characterization of MEMS piezoresistive pressure sensors fabricated by Melexis, aiming to evaluate their behaviour under mechanical stress. The main challenge addressed is the accurate measurement of resistance variation in piezoresistors under strain, a key parameter for evaluating sensor performance. The problem is particularly relevant due to the adoption of a common node configuration, designed to mitigate thermal drift and packaging stress, unlike the traditional Wheatstone bridge. This configuration presents advantages in automotive applications but requires rigorous validation.

The approach involved current-voltage (I-V) characterization of the sensors, four-point bending tests to induce mechanical strain, and the design of both manual and automatic interface circuits for resistance measurement. Resistance changes and gauge factors were extracted and compared against theoretical expectations for silicon-based piezoresistors. Baseline resistance values ranged from 5.21 kΩ to 5.37 kΩ with less than 2% variation. Under applied strain, longitudinal piezoresistors A2 and B2 exhibited experimental gauge factors of 67.9 and 17.4, respectively, which is substantially lower than the theoretical value of 130 for p-type silicon in the <110> direction.

The results revealed significant inconsistencies, including unexpected resistance behaviour, high relative errors, and limited sensitivity to mechanical stress. After systematic testing of all components, a design error in the manual switch PCB, specifically, an incorrect FPC pin mapping, was identified as the likely cause of measurement anomalies. This work highlights the importance of reliable measurement infrastructure in sensor characterization. Despite deviations from expected behaviour, the developed methodology and analysis provide a solid foundation for future improvements in MEMS sensor testing and validation.

Keywords: MEMS, piezoresistive pressure sensor, gauge factor, four-point bending, sensor characterization, interface circuit.

RESUMO

Os sensores de pressão piezoresistivos baseados em MEMS (Sistemas Microeletromecânicos) são amplamente utilizados em setores como o automotivo, biomédico e de automação industrial, onde alta sensibilidade, compacidade e baixo consumo energético são essenciais. Esta dissertação tem como foco a caracterização de sensores piezoresistivos MEMS fabricados pela Melexis, com o objetivo de avaliar seu comportamento sob tensão mecânica. O principal desafio abordado é a medição precisa da variação de resistência dos piezoresistores sob deformação, um parâmetro crítico para a avaliação do desempenho do sensor. O problema é especialmente relevante devido à adoção de uma configuração de nó comum, projetada para mitigar deriva térmica e tensões de encapsulamento, ao contrário da tradicional ponte de Wheatstone. Embora vantajosa em aplicações automotivas, esta configuração exige validação experimental rigorosa.

A metodologia adotada envolveu a caracterização corrente-tensão (I-V) dos sensores, testes de flexão em quatro pontos para indução de tensão mecânica e o desenvolvimento de circuitos de interface, manuais e automáticos, para medição de resistência. As variações de resistência e os fatores de gauge foram extraídos e comparados com os valores teóricos esperados para piezoresistores de silício. Os valores de resistência inicial variaram entre 5,21 kΩ e 5,37 kΩ, com menos de 2% de variação. Sob esforço mecânico, os piezoresistores longitudinais A2 e B2 apresentaram fatores de gauge experimentais de 67,9 e 17,4, significativamente inferiores ao valor teórico de 130 para silício tipo p na direção <110>.

Os resultados revelaram inconsistências significativas, como comportamento anômalo da resistência e baixa sensibilidade à deformação. Após testes sistemáticos, identificou-se um erro de projeto na placa de circuito impresso manual como causa provável. Apesar dessas limitações, a metodologia desenvolvida oferece uma base sólida para futuras melhorias na caracterização e validação de sensores MEMS.

Palavas chave: MEMS, sensor de pressão piezoresistivo, factor de sensibilidade, flexão em quatro pontos, caracterização de sensores, circuito de interface.

CONTENTS

1 MOTIVATION 1
2 INTRODUCTION 2
2.1 Piezoresistivity 2
2.2 Piezoresistive Coefficients 3
2.3 Gauge Factor 4
2.4 MEMS piezoresistive pressure sensors 4
2.4.1 Wheatstone Bridge configuration 4
2.4.2 Common node configuration 5
2.5 Challenges and Advancements in MEMS Piezoresistive Pressure Sensors 6
3 METHODS AND MATERIALS 7
3.1 Wafer and Sample Overview 7
3.2 I-V Curve Characterization 7
3.3 Sample Mounting and Wire Bonding 7
3.4 Four-Point Bending Setup 7
3.4.1 Measurement Setup 8
3.4.2 Resistance Measurements 8
3.5 Interface Circuit Development 8
4 RESULTS AND DISCUSSION 9
4.1 Wafer and Sample Overview 9
4.2 I-V Curve Characterization 10
4.3 Four-Point Bending 11
4.3.1 Experimental Setup and Methodology 11
4.3.2 Testing Protocol 12
4.3.3 Testing Limitations 12
4.4 Carrier PCB 13

4.5 Manual Switch PCB 15
4.6 Resistance Analysis 16
4.7 Relative Resistance Change Analysis 18
4.7.1 Gauge factor analysis 19
4.8 Interface Circuit Testing 21
4.9 Automatic Interface Circuit PCB 23
4.9.1 Implementation 25
4.9.2 Testing 26
5 CONCLUSION AND FUTURE PROSPECTS 29
6 BIBLIOGRAPHY 31
7 ANNEX A - 3D PIECE DESIGN 34
8 ANNEX B - RESISTANCE ANALYSIS 36
9 ANNEX C - GAUGE FACTOR ANALYSIS 41
10 ANNEX D - ARDUINO CODE 44

LIST OF FIGURES

Figure 1 - Wheatstone Bridge configuration [4] 5
Figure 2 - Schematic top view of the MEMS pressure sensor layout featuring a common node configuration, showing piezoresistors located on the membrane (R_{Tmemb}, R_{Lmemb}) and on the reference frame (R_{Tref}, R_{Lref}) for differential stress sensing [14] 6
Figure 3 - (a) Setup used for the I-V curve characterization; (b) Setup used for the four-point bending measurements 8
Figure 4 - Sensor layout with each pad represented 9
Figure 5 – (a) I-V curve of sample 1; (b) I-V curve of sample 2; 10
Figure 6 - Sample on the clamp setup after being wire bonded, with the location of the samples wire bonded shown in the legend. 11
Figure 7 - Four-point bending configuration used. 12
Figure 8 – Layout of the carrier PCB designed 14
Figure 9 - Representation of a sample wire bonded on Position A 14
Figure 10 - Top view of manual switch PCB designed 15
Figure 11 - Resistance (kΩ) variation with applied stress (MPa) across position B in sample 1, sample 2, sample 3 and sample 4 for: (a) piezoresistor A1, (b) piezoresistor A2, (c) piezoresistor B1, (d) Piezoresistor B2. 16
Figure 12 - Relative resistance change (%) in function of strain (%) across position B in sample 1, sample 2, sample 3 and sample 4 for: (a) piezoresistor A1, (b) piezoresistor A2, (c) piezoresistor B1, (d) piezoresistor B2. 18
Figure 13 - Setup used to test: (a) the carrier PCB; (b) the manual switch PCB 21
Figure 14 - Setup used to test the carrier PCB and manual switch PCB connection 22
Figure 15 - FPC schematic connections of manual switch PCB (See section 4.5) 22
Figure 16 - Top view of the automatic switch PCB 24
Figure 17 – Example of an SPI Communication Waveform: Data Transfer between Master and Slave (Mode 0) [30] 25
Figure 18 - Timing diagram of the signals from digital pins 2,3,4,5,6,11,12 and 13 from Arduino Uno board. 26
Figure 19 - Setup used to test the automatic switch PCB directly with the samples 27
Figure 20 - Schematic of the automatic switch PCB 27
Figure 21 - 3D piece used for inner support on the four-point bending setup. 34

Figure 22 - (a) old design of 3D Piece for outer support; (b) new design for 3D piece for outer support. 34
Figure 23 - 3D piece design for outer support of the four-point bending setup with 30 mm contact distance 35
Figure 24 – Resistance (kΩ) in function of stress (MPa) across position A in sample 1, sample 2 for: (a) piezoresistor A1, (b) piezoresistor A2, (c) piezoresistor B1, (d) piezoresistor B2. 36
Figure 25 –Resistance (kΩ) in function of stress (MPa) across position C in sample 1, sample 2 for: (a) piezoresistor A1, (b) piezoresistor A2, (c) piezoresistor B1, (d) piezoresistor B2. 37
Figure 26 –Resistance (kΩ) in function of stress (MPa) across position D in sample 1, sample 2 for: (a) piezoresistor A1, (b) piezoresistor A2, (c) piezoresistor B1, (d) piezoresistor B2. 38
Figure 27 - Relative resistance change in function of strain (%) across position A for sample 1, sample 2, sample 3 and sample 4 for: (a) piezoresistor A1, (b) piezoresistor A2, (c) piezoresistor B1, (d) piezoresistor B2. 41
Figure 28 - Relative resistance change in function of strain (%) across position C for sample 1, sample 2, sample 3 and sample 4 for: (a) piezoresistor A1, (b) piezoresistor A2, (c) piezoresistor B1, (d) piezoresistor B2. 42
Figure 29 - Relative resistance change in function of strain (%) across position D for sample 1, sample 2, sample 3 and sample 4 for: (a) piezoresistor A1, (b) piezoresistor A2, (c) piezoresistor B1, (d) piezoresistor B2. 42

LIST OF TABLES

Table 1 - Dimensions of samples 1,2,3 and 4. 10
Table 2 - Resistance values obtained from the I-V curves in Figure 3(a) and Figure 3(b) 11
Table 3 - Maximum number of weights that can be used for each sample before permanent deformation of the piezoresistors. 13
Table 4 - Comparison between resistance values at minimum stress obtained from Figure 8 and resistance values without applied stress from Table 2. 17
Table 5 - Comparison between experimental longitudinal gauge factor and theorical longitudinal gauge factor 20
Table 6 - Resistance range obtained from theorical longitudinal gauge factor from the values on Table 2 20
Table 7 - Experimental and theorical comparison of resistance values of a through hole resistor......... 21
Table 8 - Summary of the tests performed on the PCB's. 23
Table 9 - Comparison between experimental longitudinal gauge factor and theorical longitudinal gauge factor for positions A, C and D.. 43

ACRONYMS

MEMS	Microelectromechanical Systems
CAGR	Compound Annual Growth Rate
GF	Gauge Factor
IPA	Isopropyl Alcohol
PCB	Printed Circuit Board
FPC	Flexible Printed Circuit
I-V	Current-Voltage
GND	Ground
SPI	Serial Peripheral Interface
VDD	Voltage Supply
VLOGIC	Logic Voltage Supply
SPI	Serial Peripheral Interface
CLK	Clock.
MOSI	Master Out Slave In
MISO	Master In Slave Out
CS/SS	Chip Select / Slave Select

SYMBOLS

ε	Strain
σ	Applied stress
R_0	Initial resistance
R	Resistance after deformation
ρ	Electrical resistivity
ρ_0	Initial resistivity
π	Piezoresistive coefficient
π_{11}, π_{12}, π_{44}	Specific piezoresistive tensor coefficients for cubic semiconductors
τ_k	Stress tensor components
E	Young's modulus
GF	Gauge factor
GF_L	Longitudinal Gauge Factor
V	Voltage
I	Current
l	Length
w	Width
t	Thickness
g	Gravitational acceleration

1 Motivation

MEMS are reshaping the technological landscape, driving innovation across multiple industries. Among these, the automotive sector stands out as a key beneficiary of MEMS development, particularly in the field of pressure sensing. MEMS pressure sensors, with their miniaturized footprint, high sensitivity, and low power consumption, are vital components in safety systems, engine control, and tire pressure monitoring [1-2]. Their widespread adoption is not merely a technical improvement, but it represents a significant engine of economic growth and industrial modernization.

Recent market analyses underscore this trend. The global MEMS pressure sensors market is projected to grow at a CAGR of 8.9%, from US$5.2 billion in 2023 to US$9.5 billion by 2030, fueled by the adoption of IoT, automotive electrification, and wearable medical devices [3]. Furthermore, the broader MEMS sensor market was expected to exceed $100 billion in revenue by 2023, reinforcing its pivotal role in the evolution of Industry 4.0 [1].

This technological boom also intensifies competition. Industry giants such as Bosch Sensortec, Honeywell, and STMicroelectronics continue to innovate aggressively, developing increasingly compact, durable, and multi-functional pressure sensors. For a company like Melexis, which specializes in advanced automotive semiconductors, this competitive landscape has catalyzed a strategic response: the development of next-generation embedded pressure sensors tailored to the specific demands of modern vehicles.

Melexis, based in Belgium, has maintained a strong position in automotive sensor solutions, with an average of over 18 chips per vehicle globally in 2023. However, the rise of electric vehicle adoption, autonomous driving, and stricter emission regulations has prompted the company to further enhance its MEMS pressure sensing technologies. Recent product launches, including pressure sensors specifically designed for engine management and battery thermal regulation, are clear responses to emerging market needs and competitive challenges.

Research into advancements in material science, such as biocompatible coatings and silicon-based piezoresistive structures, has significantly improved the performance of MEMS sensors in harsh automotive environments. These innovations provide greater stability, precision, and miniaturization - qualities that are increasingly demanded by vehicle manufacturers.

This thesis is motivated by the convergence of several factors: the robust market growth of MEMS sensors, the essential role of pressure sensing in automotive innovation, and the competitive pressure on industry leaders like Melexis to innovate. By focusing on the design and optimization of MEMS pressure sensors for automotive applications, this research aims to contribute to the technological advancement of safe, efficient, and intelligent mobility solutions.

2 | INTRODUCTION

MEMS piezoresistive pressure sensors are among the most widely used pressure-sensing technologies due to their high sensitivity, simple design, and ease of integration with electronic systems [4]. These devices measure a pressure signal and convert it into an output electric signal, according to a specific transducing principle.

One of the most common transduction principles used is piezoresistive sensing, where changes in mechanical strain result in variations in electrical resistance [4].

2.1 Piezoresistivity

Piezoresistivity is characterized by the change in the electrical resistivity of a material due to applied mechanical stress.

Equation 1 describes the resistance of a filament with length (l_0), width (w_0) and thickness (t_0) with a given resistivity (ρ_0), when no stress is applied to it [5].

$$R_0 = \rho_0 \frac{l_0}{t_0 w_0} \tag{1}$$

When such a filament suffers strain (ε), described by Equation 2, the resistor dimensions, namely the length (l), width (w) and thickness (t), as well as resistivity (ρ), change. This change can be described by Equation 3, which explains what happens to a filament after being subjected to strain [5].

$$\varepsilon = \frac{l - l_0}{l} \tag{2}$$

$$R_{stressed} = \frac{l}{w.t}\rho \tag{3}$$

$$\frac{\Delta R}{R_0} = (1 + 2\nu)\varepsilon + \frac{\Delta\rho}{\rho_0} \tag{4}$$

The relative resistance change can be then describe by Equation 4, where $\nu = -\varepsilon_{transversal}/\varepsilon_{longitudinal}$ is the Poisson's ratio, R_0 is the initial resistance and $\Delta R = R_{stressed} - R_0$, with $R_{stressed}$ being the resistance after suffering deformation.

Equation 4 can be divided into two terms, with the first term originating from geometric changes in resistance due to stress. In contrast, the second term is caused by changes in resistivity due to piezoresistivity. In the case of metals under stress, the geometric changes (first term) are dominant, with minimal influence from the changes in resistivity (second term). However, in

semiconductors like silicon and germanium, the resistivity changes (second term) are more significant since stress-induced modifications to the electronic band structure lead to variations in charge carrier mobility and concentration, making the geometric effects negligible [6].
Silicon, a key semiconductor, has a diamond cubic structure. When stress is applied, it disrupts the lattice symmetry, altering atomic positions and energy levels in the conduction and valence bands. This shift redistributes electrons, affecting their effective mass and mobility, which varies with the stress orientation due to silicon's anisotropic band structure. [4,7]. These changes in carrier mobility lead to a change in the resistivity[8]. Therefore, the piezoresistive effect manifests as a measurable change in resistivity, through a second-rank tensor, $\Delta\rho_{ij}/\rho$ described in Equation 5, where π_{ijkl} is the piezoresistance tensor and τ_{kl} is the stress tensor [9].

$$\frac{\Delta\rho_{ij}}{\rho} = \sum_{k,l} \pi_{ijkl}\tau_{kl} \tag{5}$$

2.2 Piezoresistive Coefficients

For anisotropic materials, such as silicon, resistivity is a second-rank tensor described by a 3x3 matrix, therefore, Equation 5 can be written as Equation 6. In the same equation, the stress tensor (τ_k) has 9 components, however, due to the symmetry of shear stress components, it only has 6 independent components. π_{ik} is a 6x6 matrix, which takes the form of Equation 7 for cubic semiconductors [9-10].

$$\frac{\Delta\rho_{i}}{\rho} = \sum_{k=1}^{6} \pi_{ik}\tau_{k} \tag{6}$$

In cubic semiconductors like silicon, many of these coefficients are zero or equal due to crystal symmetry, resulting in the presence of only three independent components, π_{11}, π_{12} and π_{44} [9], [10]. Each of these coefficients represents a distinct aspect of the piezoresistive effect. π_{11} describes the longitudinal piezoresistive effect, where resistance changes along the direction of applied stress; π_{12} accounts for the transverse piezoresistive effect, where resistance changes perpendicular to the applied stress; and π_{44} characterizes the shear piezoresistive effect, which influences out-of-plane electric fields due to in-plane shear stress [9,11].

$$\pi_{ik} = \begin{pmatrix} \pi_{11} & \pi_{12} & \pi_{12} & 0 & 0 & 0 \\ \pi_{12} & \pi_{11} & \pi_{12} & 0 & 0 & 0 \\ \pi_{12} & \pi_{12} & \pi_{11} & 0 & 0 & 0 \\ 0 & 0 & 0 & \pi_{44} & 0 & 0 \\ 0 & 0 & 0 & 0 & \pi_{44} & 0 \\ 0 & 0 & 0 & 0 & 0 & \pi_{44} \end{pmatrix} \tag{7}$$

2.3 Gauge Factor

Equation 8 describes the measurement of relative change in resistance using the Gauge factor (GF) [4-5,9,11].

$$\frac{\Delta R}{R_0} = (1 + 2\nu + \pi E)\varepsilon = GF.\varepsilon \tag{8}$$

According to Equation 8, the larger the GF, the more significant the resistance change with the material's elongation. For most metals, π is negligible and the GF is determined by the geometric resistance change of the resistor [9].

Metals usually display a gauge factor value between 2 and 5, while semiconductor materials have values 50 to 100 times bigger than that. Silicon p-type can present values of 130 and up to 200 [4-6,12-13].

However, for most MEMS applications, materials are selected to achieve a GF typically 10 to 100 times bigger than the resistance change caused by the geometric change, with the sensitivity of these devices usually related to this figure of merit [5]. This makes semiconductors like silicon suitable materials for MEMS applications.

In crystalline semiconductors, the doping level, doping type, and the crystallographic direction in which tensile or compressive stress is applied, strongly influence the longitudinal and the transversal gauge factors [6,12].

2.4 MEMS piezoresistive pressure sensors

As previously explained, MEMS pressure sensors use the piezoresistive effect to convert mechanical strain induced by the deformation of a diaphragm into an electrical signal. So, one of the key elements of these sensors is the diaphragm, which is generally made from single-crystal silicon and is designed to be thin enough to deform with the application of pressure while maintaining the integral structure [6]. The other key components are the piezoresistors that detect pressure-induced deflection. These are usually placed in high strain regions to ensure that the resistance changes are maximized in response to diaphragm deformation, enhancing the sensor's accuracy and sensitivity [8,11]. With these two key elements, the resistance changes are measured using a certain configuration, usually a Wheatstone bridge, providing an electrical output proportional to the applied pressure [4].

2.4.1 Wheatstone Bridge configuration

A Wheatstone bridge configuration is usually used in MEMS piezoresistive pressure sensors, as it efficiently converts small resistance variations into a measurable voltage signal. As seen in Figure 1, the bridge consists of four piezoresistive elements arranged in a square configuration. Two resistors are subjected to compressive strain (R_C), while the other two experience tensile strain (R_T). The Wheatstone bridge is usually used in differential configurations to enhance the sensitivity of the sensor and mitigate errors caused by temperature fluctuations [4].

$$V_{out} \approx (\frac{\Delta R}{R})V_{in} \quad (9)$$

Considering R_T and R_C as the resistances of the tensile and compressive piezoresistors, respectively, and V_{in} the supply voltage applied to the bridge, then assuming $R_T = R + \Delta R$ and $R_C = R - \Delta R$, for small changes in resistance (ΔR), the output voltage can be approximated by Equation 9 [6,9,11].

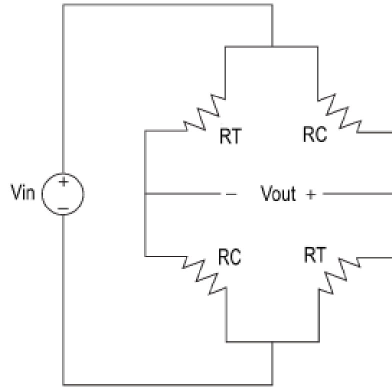

Figure 1 - Wheatstone Bridge configuration [4].

2.4.2 Common node configuration

Although the Wheatstone bridge is commonly used, some companies, such as Bosch and Honeywell, are exploring an alternative approach known as the common node configuration. This variation, patented by Melexis [14] and used in the samples analyzed in the following sections, consists of two resistors with different orientations placed on the membrane, along with two piezoresistors oriented differently on the frame, as presented in Figure 2. As seen in Figure 2, the sensing resistors on the membrane primarily respond to applied pressure, while the reference resistors are designed to remain largely unaffected by pressure. However, they still experience the same environmental disturbances, such as packaging stress or thermal drift. This configuration enables the system to differentiate between true pressure-induced signals and parasitic effects. Additionally, it compensates for thermal loads, a capability that is lacking in a traditional Wheatstone bridge due to its high sensitivity.

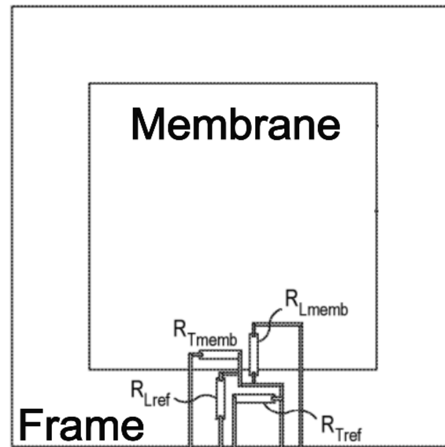

Figure 2 - Schematic top view of the MEMS pressure sensor layout featuring a common node configuration, showing piezoresistors located on the membrane (R_{Tmemb}, R_{Lmemb}) and on the reference frame (R_{Tref}, R_{Lref}) for differential stress sensing [14].

2.5 Challenges and Advancements in MEMS Piezoresistive Pressure Sensors

MEMS piezoresistive pressure sensors have had significant advancements, leading to their widespread application in the medical, automotive, and industrial sectors [1]. Their compact size, high sensitivity, and compatibility with microelectronics make them essential for monitoring [8].
Despite their benefits, piezoresistive sensors face challenges, including temperature-induced drift, adhesive-induced stress, and material reliability. One of the main challenges is temperature-induced drift, which compromises sensor accuracy across a wide range of operating conditions [15]. Fluctuations in the resistivity of piezoresistive materials due to temperature changes can lead to variations in the output signal. Although compensation techniques, such as temperature calibration and advanced signal processing algorithms, have been developed, eliminating drift remains challenging [16]. Another significant issue is package induced stress. The adhesives used to bond MEMS sensors to packaging structures or substrates can experience mechanical stress due to differences in thermal expansion coefficients, resulting in hysteresis effects and long-term instability. This also happens to the packaging material itself [17-18]. Ongoing research focuses on developing new bonding techniques, including direct wafer bonding and low-stress adhesives [19]. In addition to this, there is still a pressing demand for higher sensitivity, a broader pressure range, and enhancements in factors such as sensitivity, stability, and power consumption [1,20].
Given the ongoing challenges and demands in MEMS piezoresistive pressure sensor technology, this study investigates MEMS piezoresistive pressure sensors featuring a common node configuration developed by Melexis, with a focus on accurately determining the gauge factor of fabricated samples. By characterizing this parameter, the work aims to evaluate the sensitivity and performance implications of this architecture. The results are intended to support the development of next-generation pressure sensors and contribute to the Melexis portfolio of advanced sensing technologies.

3 METHODS AND MATERIALS

3.1 Wafer and Sample Overview

The samples analyzed in this study were diced from an 8-inch wafer supplied by Melexis. This wafer was fabricated to contain multiple MEMS pressure sensors, with either a common node configuration or a Wheatstone bridge configuration. A total of four samples were selected for characterization in this study.

3.2 I-V Curve Characterization

In order to find reference values for the resistance measured, I-V curves were constructed using a probe station setup presented in Figure 3(a). It is important to state that no stress was applied. A Keithley 2604B Source Meter generated a voltage sweep from -10 V to +10 V in 1 V steps. For each step, 50 current values were recorded. The resistance from the four piezoresistors of a sensor from samples 1 and 2 was measured.

3.3 Sample Mounting and Wire Bonding

The samples were diced from the wafer using a DAD323 dicing saw with a ZH05-SD3000-N1-70 diamond blade. Following dicing, the samples were cleaned with isopropyl alcohol (IPA) to remove residual debris.
After dicing, the samples were placed onto a custom-designed carrier PCB. Using a clamp fixture, which held the samples securely, they were wire bonding. Wire bonding was carried out using aluminum wires, and only four sensors were bonded to each sample.

3.4 Four-Point Bending Setup

The wire-bonded samples were tested using a four-point bending setup designed to measure sensor response under stress. The setup consisted of two 3D-printed pieces, one for the bottom layer and another one for the top layer (see annex A) designed in Solid Edge, which applied controlled contact points for bending the sensor. The distance between the contact points of the top 3D piece and the bottom 3D piece was maintained for every measurement made. To start mounting the setup for the four-point bending the bottom 3D piece was fixed in place with screws. The carrier PCB with the wire bonded sample was inserted into the setup, ensuring that the PCB's designed hole aligned with the bottom 3D piece's heaves that make the contact points, without causing friction.

(a)

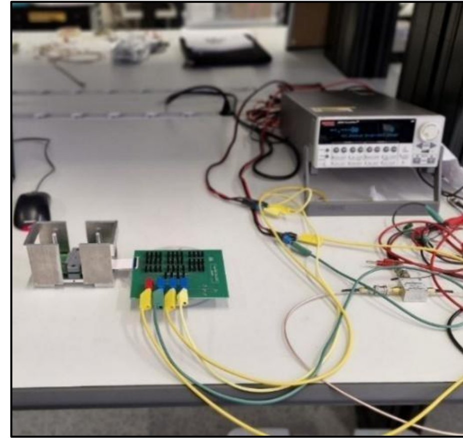

(b)

Figure 3 - (a) Setup used for the I-V curve characterization; (b) Setup used for the four-point bending measurements.

3.4.1 Measurement Setup

To measure the resistance of the piezoresistors, the carrier PCB was connected to a manual switch PCB via flexible printed circuit (FPC) connectors. The electrical characterization was carried out using a Keithley 2604B Source Meter in ohmmeter mode, supplying 5 V and limiting the current to 0.5 mA. The source meter was connected to the manual switch PCB with the positive terminal (V+) of channel A on the source meter was connected to the V+ banana connector of the manual switch PCB and the negative terminal (V-) of channel A was connected to the V- banana connector of the manual switch PCB. This setup can be observed in Figure 3(b).

3.4.2 Resistance Measurements

Resistance values were recorded under various loading conditions. Incremental loading involved taking measurements progressively after additional weights were added on top of the 3D-printed piece. Approximately 150 resistance values were recorded for each added weight. The rest of the procedure was maintained for every sample.

3.5 Interface Circuit Development

An interface circuit was also developed to allow more automatic switching between sensor channels. This circuit used switches controlled by an Arduino Uno board where SPI communication was implemented to allow for more automatic switching. The circuit was powered by two Agilent E3610A units providing 12V for VDD, 3.3V for V_{LOGIC}, and a Keithley 2604B source meter to power the PCB. The interface circuit was tested using custom Arduino code which could select specific switches and channels via user input (See annex D), and the same setup observed in Figure 3(b), with the only difference being the substitution of the manual switch PCB, detailed in section 4.5, for the automatic switch PCB, detailed in section 4.9.

4
Results and Discussion

4.1 Wafer and Sample Overview

As previously stated, the samples analyzed in this study were diced from an 8-inch wafer supplied by Melexis. This wafer was fabricated to contain multiple MEMS pressure sensors with only two different configurations, Wheatstone bridge and common node.

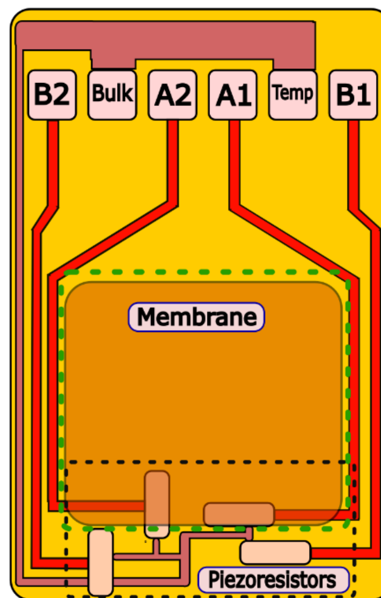

Figure 4 - Sensor layout with each pad represented.

Each sample each contains four rows of MEMS sensors. Each sample was diced from a (100) surface main. It is important to note that after getting diced from the main wafer the samples were diced again to fit the carrier PCB (See section 4.4) designed for the four-point bending setup.
Each sensor on the samples featured six different pads. Figure 4 presents a schematic of a sensor and the respective piezoresistors and designated pads, as well as the membrane's location. A1 is a longitudinal piezo-resistor positioned on the membrane. A2 is a transversal piezoresistor also positioned on the membrane. B1 and B2 are both fixated on the frame of the sensor, with B1 being a transversal piezoresistor and B2 being a longitudinal piezoresistor. Other useful pads are the Bulk, which is the primary voltage/current supply pad and Temp corresponds to the temperature sensor pad, though it was not used in this study. Each sensor analyzed has a common node configuration.
It is also important to state that in every measurement that used a current source and a multimeter, the positive terminal of the device was always connected to the bulk pad while the GND terminal was always connected to one of the piezoresistors' pads.

Each sensor consists of a membrane and piezoresistors made of silicon. Table 1 presents the dimensions of each sample, which were measured using a digital caliper. Although the samples are trapezoidal, we simplified the analysis by approximating them as rectangular shapes.

Table 1 - Dimensions of samples 1,2,3 and 4.

Sample number	Sample Thickness (mm)	Width (mm)	Length (mm)
1	0.56	5.62	56.23
2	0.56	5.62	56.23
3	0.55	5.92	59.79
4	0.55	5.94	69.48

4.2 I-V Curve Characterization

In order to characterize the sensors, the piezoresistive effect must be tested. For this, the resistance should be measured without any stress applied to the samples. I-V curves were obtained voltage sweep from -10 V to +10 V in 1 V steps, with 50 current values recorded in each step, as specified in section 3.2.
The current-voltage characterization results for Samples 1 and 2 are illustrated in Figure 5(a) and Figure 5(b), respectively.

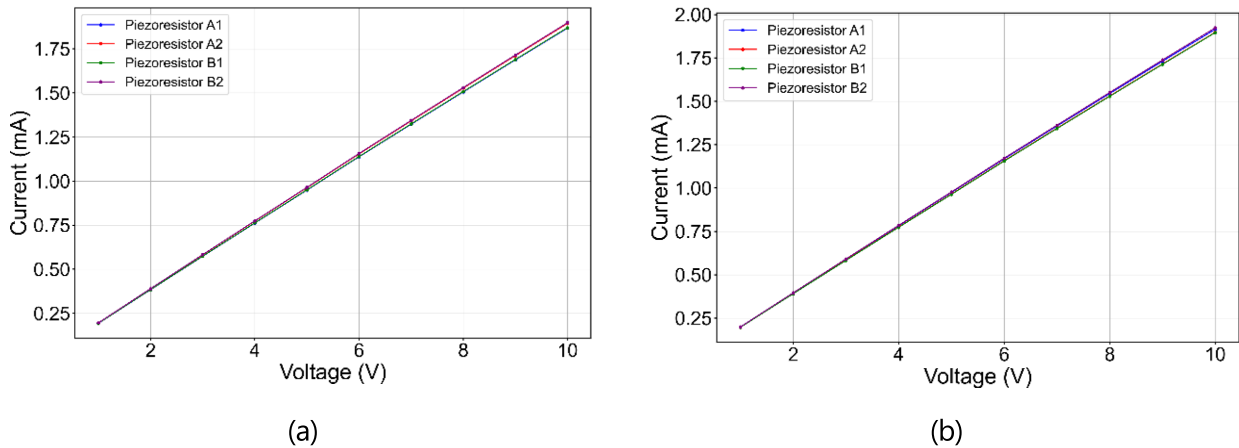

Figure 5 – (a) I-V curve of sample 1; (b) I-V curve of sample 2;

From these curves, the resistance of the devices was extracted considering negligible contact resistance and leading to an average resistance of 5.29 ± 0.05 kΩ. The individual resistance values are present in Table 2.

Table 2 - Resistance values obtained from the I-V curves in Figure 5(a) and Figure 5(b).

Sample	Resistor	Resistance (kΩ)	Average Resistance (kΩ)
1	A1	5.37	5.29 ± 0.05
	A2	5.30	
	B1	5.37	
	B2	5.28	
3	A1	5.24	
	A2	5.29	
	B1	5.29	
	B2	5.21	

In the two samples analyzed, the resistance of each of the same piezoresistors showed a maximum variation of approximately 2%, indicating high consistency between sample measurements.

4.3 Four-Point Bending

4.3.1 Experimental Setup and Methodology

To assess the properties of the MEMS pressure sensor, four samples were examined to confirm their piezoresistive functionality. The MEMS samples were wire bonded to a carrier PCB with aluminum wires. After wire bonding, each sample has four sensors, located in positions A, B, C, and D, as presented in Figure 6, connected via aluminum wires to the carrier in four different locations. This designation is particularly relevant in the four-point bending test, where the distance between the position and the contact points significantly influences bending and stress distribution [21]. However, in order to determine the strain and stress on the samples, some approximations were made that disregarded the non-uniform stress and strain behaviour along the sample, considering it uniform.

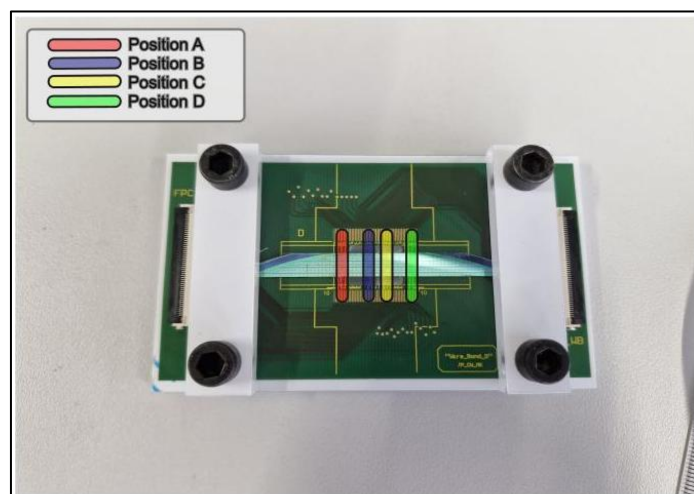

Figure 6 - Sample on the clamp setup after being wire bonded, with the location of the samples wire bonded shown in the legend.

As shown in Figure 7, in this configuration of the four-point bending test, the specimen is supported at two inner points, while the load is applied at two outer points, resulting in a zone of constant bending moment between these loading points.

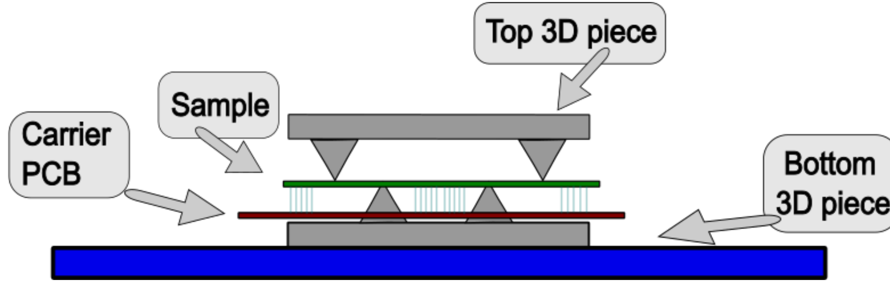

Figure 7 - Four-point bending configuration used.

This arrangement allows for the evaluation of material behavior under pure bending conditions, effectively minimizing shear forces in the area between the loading pins.
For both the inner and outer supports, it was employed 3D-printed components made from Formlabs Grey Resin, a material with a Young's modulus of around 2.6 GPa, which is similar to that of silicon. This selection ensured mechanical uniformity with both the membrane and the piezoresistor. These 3D components served as the contact points on the sample.

4.3.2 Testing Protocol

The procedure to measure resistance is the same for all samples. As described in section 3.4, it begins with securing the 3D-printed component with the 10 mm contact distance to the bottom of the platform using the central screw. The carrier PCB containing the MEMS pressure sensor sample is positioned on the four support beams. A complementary 3D-printed component is placed on top of the PCB. Previously measured weights are manually loaded onto the top 3D-printed piece to apply the desired mechanical stress to the sensor sample. The results are recorded sequentially for each added weight.

4.3.3 Testing Limitations

To prevent the plastic deformation of the membrane and the piezoresistors, the number of weights applied during testing is determined by the yield strength of silicon. The maximum allowable stress is determined by analyzing the mechanical properties of silicon, particularly along the crystallographic orientation relevant to our samples.
Wilson *et all* [22] reported fracture strength values of approximately 1.4 to 2.3 GPa for silicon in this orientation, while Gardner *et all* [12] reported a yield strength of 6.9 GPa. Nakao *et all* [23] found that silicon microstructures with (100) orientation exhibited an average fracture strength of approximately 4.89 GPa, at room temperature, when subjected to bending stress.
Considering the specific crystal orientation of the samples, a yield strength threshold of 2.0 GPa was established based on the previous studies to prevent plastic deformation and the eventual breaking of the membrane and piezoresistors.
According to the Euler-Bernoulli beam theory, the maximum stress (σ_{max}) in the beam can be determined by the Euler beam theory through Equation 10 [24-25], where F is the applied force, measured in Newtons, L is the distance between the outer support points, measured in meters, w is the width of the beam measured in meters and t is the thickness of the beam measured in meters.

$$\sigma_{max} = \frac{3.F.L}{4.w.t^2} \qquad (10)$$

$$F = m.g \tag{11}$$

Equation 11 presents the force exerted on the sample, where F is the applied force measured in Newtons, m is the mass of the body to which the force is being applied, measured in kg, and g is the gravitational acceleration measured in m/s^2.
By substituting Equation 11 in Equation 10, Equation 12 can be obtained.

$$m = \frac{4.\sigma_{max}.w.t^2}{3.L.g} \tag{12}$$

Considering that the average weight is $W_{load} = 32{,}03g \pm 0{,}01g$, then according to Equation 13 the maximum number of weights can be found.

$$N = \frac{4.\sigma_{max}.w.t^2}{3.L.g.W_{load}} \tag{13}$$

According to the sample dimensions in Table 1, the maximum number of weights that should be used for sample 1 can be calculated according to Equation 14.

$$N = \frac{4 \times 2 \times 10^9 \times 5.62 \times 10^{-3} \times (0.56 \times 10^{-3})^2}{3 \times 23 \times 10^{-3} \times 9.81 \times 32.03 \times 10^{-3}} = 266\ weights \tag{14}$$

Similar calculations were done for the other 3 samples, according to the respective dimensions presented in Table 1. The results are presented in Table 3.

Table 3 - Maximum number of weights that can be used for each sample before permanent deformation of the piezoresistors.

	Sample 1	Sample 2	Sample 3	Sample 4
N (Maximum number of Weights)	266	266	254	219

4.4 Carrier PCB

As previously mentioned, a carrier PCB was designed to connect the samples via wire bonding.
As seen in Figure 8, the PCB features two FPC connectors: one for MEMS samples with a common node configuration, referred to as FPC_CM, which is the configuration analyzed in this project, and another for a Wheatstone bridge configuration, referred to as FPC_WB, which was not used in this study.

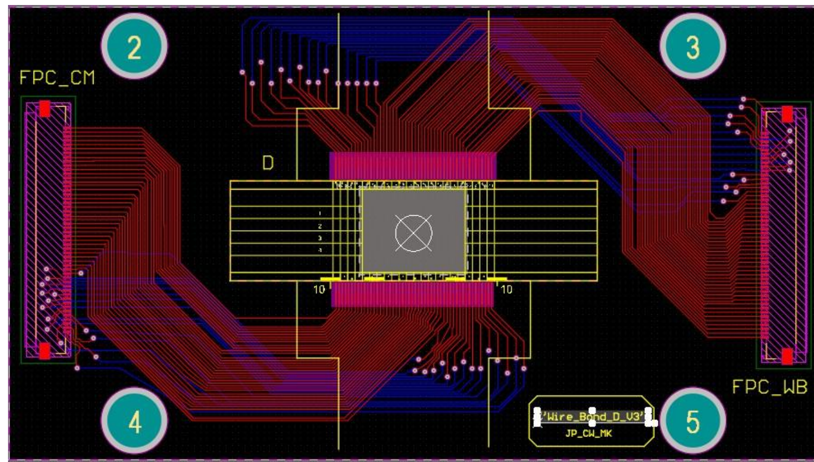

Figure 8 – Layout of the carrier PCB designed.

In the PCB layout shown in Figure 8, one of its key features is the yellow grid located in the center. This grid is designed to assist with the alignment of samples when they are mounted on the clamp setup for wire bonding. It consists of small squares, each roughly the size of an individual sensor on the MEMS sample. This design simplifies the process of aligning each sensor with the bonding pads on the PCB.

The PCB was designed to accommodate ten samples that could be wire bonded to the carrier PCB. However, due to the small size of the pads, wire bonding could only be redone a maximum of three times on each pad. To address this limitation and to improve the efficiency of the wire bonding process and testing for preliminary results, four samples were utilized.

This design incorporates a central hole, drawn to fit the heaves of the bottom piece of the four-point bending setup. Around this hole, the wire-bonding pads were left exposed, without the top solder mask that protects PCB tracks. This design allowed aluminum wires to be bonded directly to the exposed tracks making wire bond easier.

Each bonding pad on the carrier PCB was wire-bonded to a corresponding pad on the MEMS sensor. These tracks are specifically ordered, starting from the left in the following sequence (as per Figure 9): B2-Bulk-A2-A1-B1. This happens because the wire bonding would not be possible if the wires were intertwined. If this order is not followed correctly, measurements taken when connecting the manual switch PCB will be inaccurate.

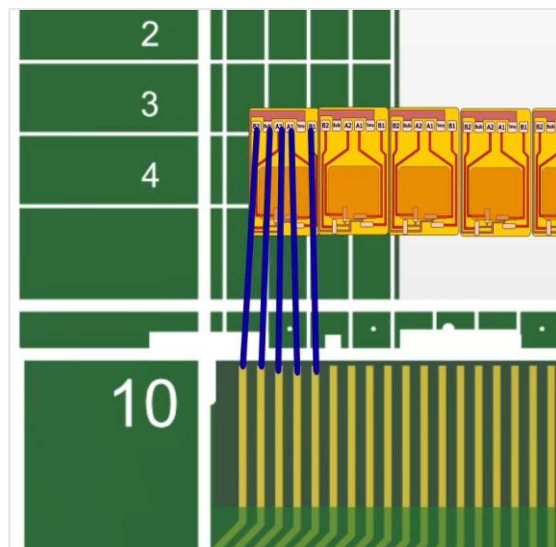

Figure 9 - Representation of a sample wire bonded on Position A.

4.5 Manual Switch PCB

This PCB was designed to select the specific resistor value to be measured by the source meter during testing. To make the electrical connections of this board to the carrier PCB, an FPC connector and cable were used as seen in Figure 10.

The main features of the PCB are the 40 slide switches. Each switch corresponds to a unique piezoresistor, with a corresponding label on top of the switch. The switches are manually operated and can be toggled between "on" and "off" positions when a desired resistor is to be measured. The instructions for these switches are displayed on the PCB in Figure 10, located in the upper right corner of the PCB.

In this setup, a constant voltage is applied to all MEMS sensors, specifically their piezoresistive elements, which share a common bulk node. This bulk node, connected through the PCB, serves as the high side (V+) of the circuit and provides the input to all the piezoresistors simultaneously.

The switches on the PCB are electronically controlled. When a switch is open (in the off state), it isolates the associated channel from the return path, effectively creating an open circuit. These open switches are not connected to ground or any low-impedance node, preventing current from flowing through their respective MEMS devices.

When a switch is turned on, it closes the conduction channel, allowing current to pass through the corresponding piezoresistor associated switch and return to the V– (negative terminal) on the PCB. This completes the circuit for that specific path. The source meter then displays the resistance of the active channel.

This selective activation enables controlled, individual electrical characterization of MEMS devices without interference from adjacent channels.

For the same reason previously explained in section 4.4, only 4 sensors were used per sample, therefore only switches 1,5,6 and 10 of the layout (see Figure 10) were used in the analysis performed.

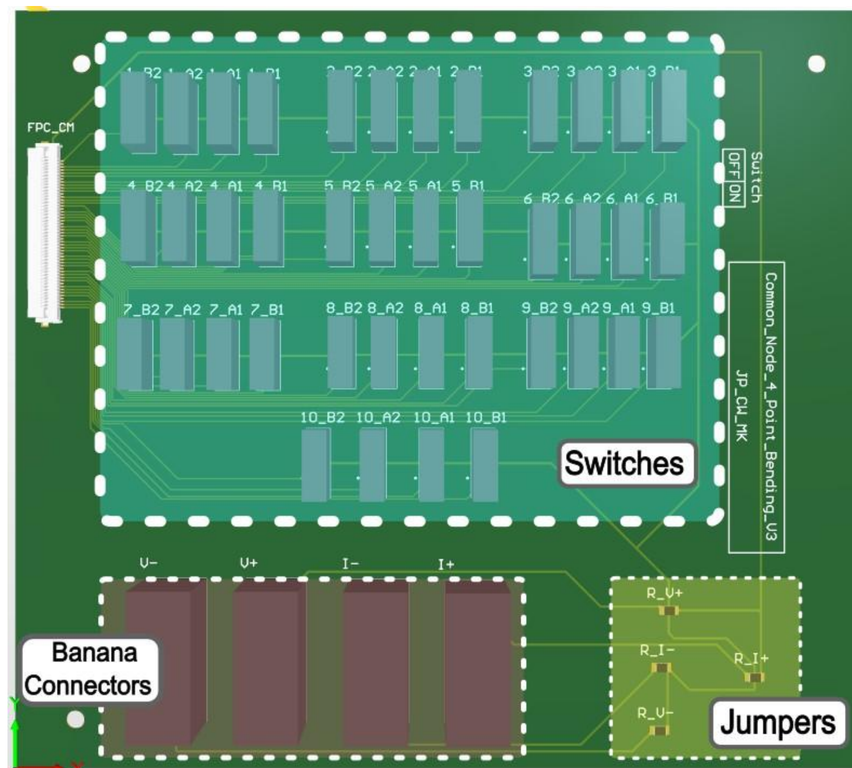

Figure 10 - Top view of manual switch PCB designed.

4.6 Resistance Analysis

As previously explained, the verification of the piezoresistors' behavior of the MEMS pressure sensor samples was performed by measuring resistance as a function of input voltage. For this, a source meter was used to input 5V and with the positive terminal connecting to the V+ entrance of the manual switch PCB and the V- connector of the manual switch PCB connecting to the negative terminal, as described in Section 3.4.2. Figure 11 shows the relationship between resistance and stress for piezoresistors A1, A2, B1, and B2 in Position B for all samples. It is important to state that stress is calculated from Equation 13, according to the number of weights used in the four-point bending measurements.

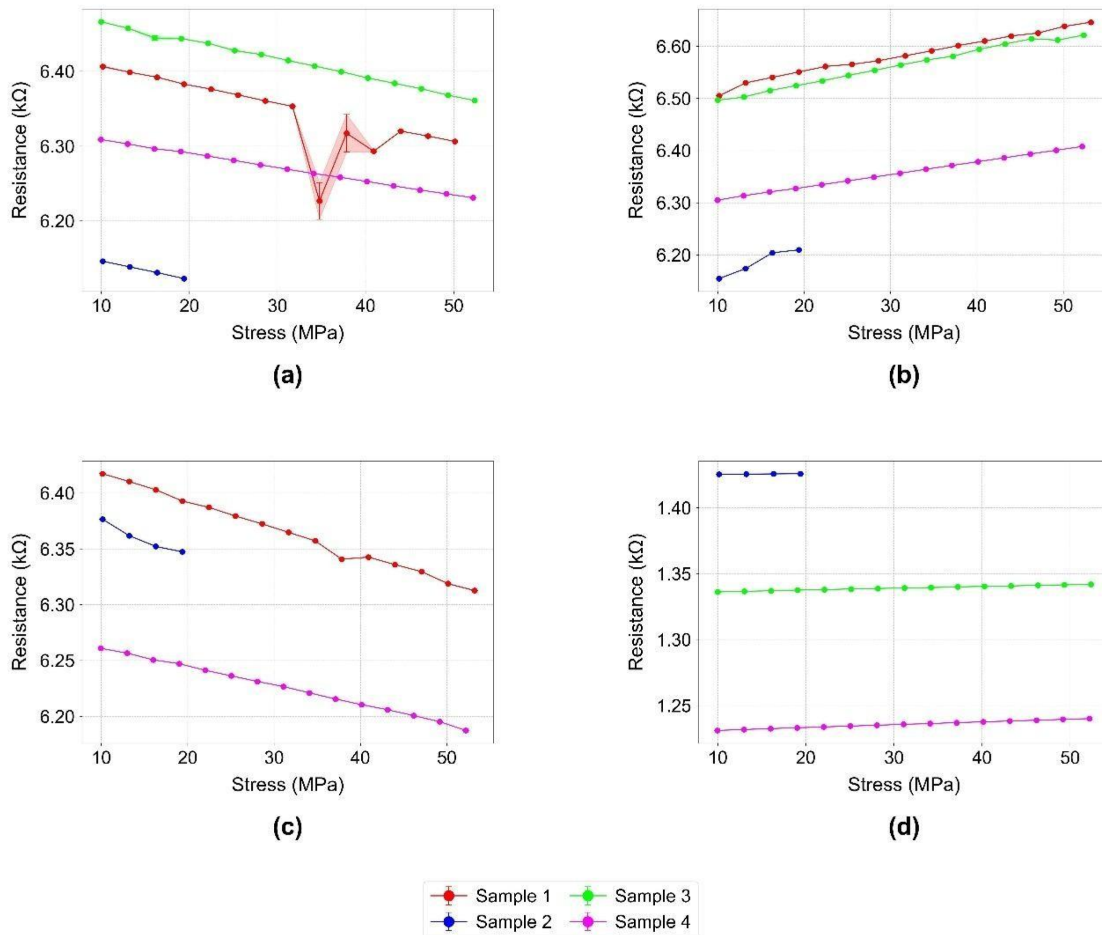

Figure 11 - Resistance (kΩ) variation with applied stress (MPa) across position B in sample 1, sample 2, sample 3 and sample 4 for: (a) piezoresistor A1, (b) piezoresistor A2, (c) piezoresistor B1, (d) Piezoresistor B2.

According to Figure 11(a), the piezoresistor A1's resistance decreases under stress for all samples. Ranging from 6.40 kΩ to 6.30 kΩ in Sample 1, while Sample 2 shows the lowest resistance, decreasing from 6.14 kΩ to 6.11 kΩ. Sample 3 has the highest values, decreasing from 6.48 kΩ to 6.35 kΩ, and Sample 4 remains the most stable, with resistance around 6.31 kΩ to 6.24 kΩ.

For piezoresistor A2, in Figure 11(b), resistance increases for all samples, with Sample 1 rising from 6.50 kΩ to 6.67 kΩ and Sample 3 following a similar trend, increasing from 6.50 kΩ to 6.62 kΩ. Sample 2 has the lowest resistance values, increasing slightly from 6.14 kΩ to 6.21 kΩ, Sample 4 rises gradually from 6.30 kΩ to 6.41 kΩ.

Presented in Figure 11(c), piezoresistor B1, resistance steadily decreases, with Sample 1 dropping from 6.40 kΩ to 6.25 kΩ, Sample 2 from 6.35 kΩ to 6.22 kΩ, and Sample 4 from 6.26 kΩ to 6.19 kΩ. Sample 1 starts

with the highest resistance, while Sample 4 has the lowest overall values. It is important to note that Sample 3 is not present in this graphic since the wire broke during measurements.
Figure 11(d) presents odd results for piezoresistor B2. Overall, resistance remains stable, with Sample 2 at 1.43 kΩ, Sample 3 bewteen 1.34 and 1.35 kΩ, and Sample 4 between 1.23 kΩ and 1.28 kΩ. B2 shows minimal variation, with Sample 2 having the highest resistance and Sample 4 the lowest. It is important to note that Sample 1 is not present in this graphic since the wire broke during measurements.
Overall, A2 increases under stress, A1 and B1 decrease, while B2 increases are minimal. Sample 1 generally shows the highest resistance, while Sample 2 presents a smaller resistance change since only four weights were used to analyze the sample in this position.
It is also important to state that from the analysis above, it is possible to confirm that each piezoresistor follows a predictable trend based on their orientation in the sensor (See Figure 4). Piezoresistors A1 and B1 decrease their resistance with stress increase due to being transversal piezoresistors, which indicates that they are subjected to compressive strain due to bending or shear deformation. As for piezoresistors A2 and B2 are longitudinal piezoresistors since they are aligned along the <110> direction, the same direction in which stress is applied to the sample. Therefore, the piezoresistive effect results in increased resistance under tensile strain. Although there is generally a linear behavior observed for the piezoresistors across all samples, which is to be expected from a piezoresistor sensor, a comparison between the resistance values obtained in the resistance vs. stress measurements and those from the I-V curve for Samples 1 and 2 (shown in Table 2) reveals a significant discrepancy. This difference suggests that some factors may be affecting the consistency and accuracy of the measurements. Table 4 presents the average lowest value measured for each piezoresistor and the relative error when compared to Table 2 resistance values.

Table 4 - Comparison between resistance values at minimum stress obtained from Figure 11 and resistance values without applied stress from Table 2.

Piezoresistor	Average Resistance from I-Curve characterization (kΩ)	Average four-point bending minimum stress resistance (kΩ)	Relative Error (%)
A1	5.31 ± 0.07	6.32315 ± 0.00001	19.16
A2	5.292 ± 0.006	6.25345 ± 0.00001	18.18
B1	5.33 ± 0.04	6.33546 ± 0.00001	18.90
B2	5.25 ± 0.04	1.316297 ± 0.000005	74.93

From Table 4, a significant relative error observed between the resistance values from the I-V curve and the four-point bending measurements can be attributed to several factors, especially in piezoresistor B2. One potential reason is the wire bonding process used to attach the sample to the carrier PCB. Although wire bonding could introduce additional resistance due to imperfect connections or contact resistance between the wires and the piezoresistors, it is not likely that the wire bonding alone could account for the significant discrepancies observed. The resistance of aluminum wire used in bonding is relatively low, and even for wires with lengths of a few millimeters, the added resistance is minimal. The resistivity of aluminum is approximately 2.82×10^{-8} Ω·m [26], and when considering bonding wire dimensions in the order of 12.5 to 500 μm in diameter, the contribution to total resistance is negligible and cannot account for such a big resistance increase.
Another contributing factor could be friction in the four-point bending setup. In this setup, friction between the beams and the top 3D piece could affect how the latter is placed, leading to an uneven distribution of stress across the sample. If the stress is not uniformly applied, it could result in localized resistance changes.

Misalignments due to friction could also affect the contact points on the sample, further distorting the measured resistance.

Temperature variations might also play a role in these discrepancies. Although the temperature was measured during the experiments and the variation registered was a maximum of 1°C, temperature fluctuations can still influence the resistance of the material, as piezoresistive behavior is temperature sensitive. However, experiments directly related to temperature effects were not conducted, so its influence on the relative error is not fully quantified.

These hypotheses were rejected since the resistance measurement error is very high, with a minimum relative error of around 16%.

4.7 Relative Resistance Change Analysis

Since the resistance values presented discrepancy and a high relative error when compared to the ones obtained from I-V curves, relative resistance change was studied. For this, the same source meter was used with an input voltage of 5 V with the positive terminal of the source meter connecting to V+ of the manual switch PCB and the negative terminal connecting to V- of the manual switch PCB.

Figure 12 presents the relative resistance change for the A1, A2, B1, B2 piezoresistors for position B in function of strain. The strain values are obtained according to Equation 15 and considering a Young's modulus of 169 GPa for silicon in the <110> direction [27-28]. It is important to note that Equation 15 relies on the approximation that strain is uniform across the sample, which is not the case. This assumption also justifies the presentation of results for only one analyzed position per sample.

$$\sigma = E\varepsilon \tag{15}$$

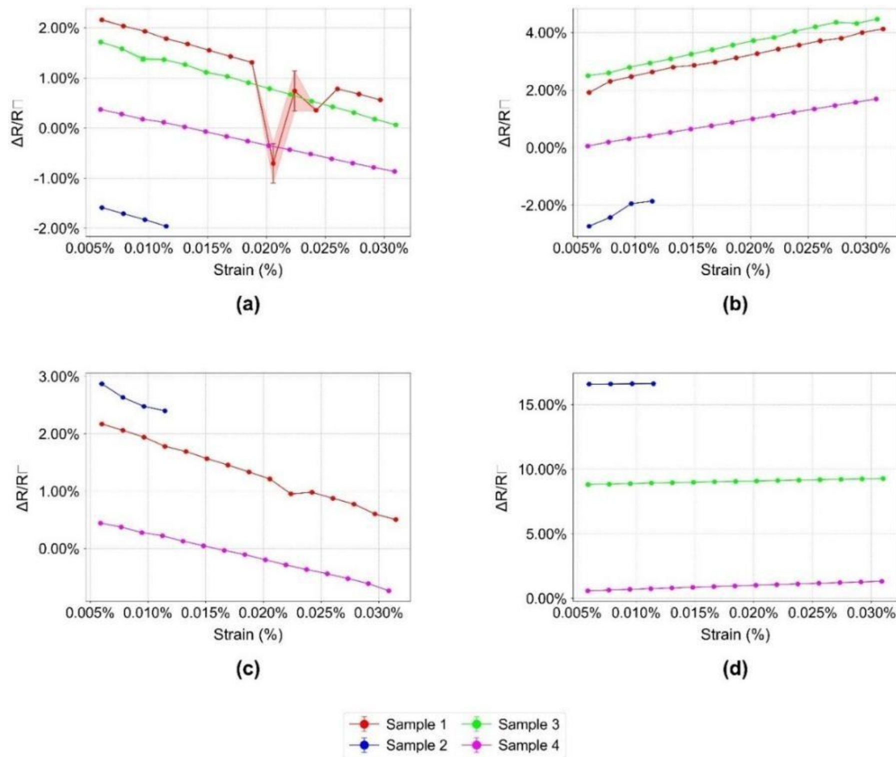

Figure 12 - Relative resistance change (%) in function of strain (%) across position B in sample 1, sample 2, sample 3 and sample 4 for: (a) piezoresistor A1, (b) piezoresistor A2, (c) piezoresistor B1, (d) piezoresistor B2.

According to Figure 12(a), piezoresistor A1 resistance variation ranges from 2.1% to 0.6% in Sample 1, showing fluctuations, while other samples exhibit more stable trends. Sample 2 shows a steady decrease from -1.6% to -2.0%, Sample 3 declines from 1.8% to 0.0%, and Sample 4 remains relatively stable (0.5% to -1.0%). Compared to the others, Sample 1 is the most unstable.
Figure 12(b) presents equivalent of the latter for Piezoresistor A2. A2's resistance increases steadily for most samples, ranging from 2.0% to 4.0% in Sample 1 and from 2.5% to 4.5% in Sample 3, while Sample 2 decreases from -3.0% to -2%. Sample 4 follows a mild increase from 0.0% to 1.8%. Among the samples, Sample 2 shows the most significant decrease, while Sample 1 has the highest overall resistance increase.
For Piezoresistor B1, as seen in Figure 12(c), resistance change decreases across all samples, with Sample 1 dropping from 2.2% to 0.5%, Sample 2 from 2.8% to 2.4%, and Sample 4 from 0.5% to -0.9. Sample 2 has the highest initial resistance change, but Sample 4 exhibits the smallest change, indicating the least sensitivity to stress.
In Figure 12(d), which corresponds to the piezoresistor B2, Sample 2 maintains a high and stable resistance variation of around 15%, while Sample 3 holds around 7.5%, and Sample 4 stays between 2.0% and 2.5%. Compared to the other piezoresistors, B2 exhibits the highest resistance variation, with Sample 2 being the most stable at a high value, while Sample 4 shows the lowest overall resistance change.
Overall, A2 shows an increasing trend, A1 and B1 decrease under stress, and B2 increases slightly. Sample 4 generally shows the least variation across all resistors.
In addition, it can also be stated that the piezoresistance orientation is demonstrated again with the slopes of each linear regression associated with the graph. With the transversal piezoresistors, A1 and B1 having a negative slope and, the longitudinal piezoresistors A2 and B2 having a positive slope.
Upon further examination of all the graphs in Figure 12, it becomes clear that there is an issue with the measurements. Some samples exhibit a null relative resistance change in response to applied strain, which is not expected behavior for a piezoresistive sensor, as previously seen in section 2.1. This is particularly evident in piezoresistors A1 and B1 for sample 4. The problem is compounded when we analyze the trend of the curves, as several others also show no resistance change with applied strain. For instance, sample 2 in piezoresistors A2 and B1, as well as samples 1 and 3 in piezoresistors 1 and 3, display the same anomaly. This further substantiates the idea that the results are inaccurate, in addition to what has already been noted with the results in Table 2.

4.7.1 Gauge factor analysis

Besides this, the gauge factor was analyzed at position B of the samples, as it serves as a more reliable figure of merit for assessing the validity of the resistance changes. Since the gauge factor relates the relative resistance change to the applied strain, its evaluation can help determine whether the resistance values from the four-point bending setup are accurate.
According to [6], the longitudinal gauge factor for p-type silicon (100) in the <110> direction is approximately 130 and usually is the most used for gauge factors analysis; therefore, only the longitudinal piezoresistors A2 and B2 will be analyzed.
With this, the slope of each graph of relative resistance change vs strain will be the gauge factor of each piezoresistor.
Table 5 presents the comparison of each average gauge factor for longitudinal piezoresistors A2 and B2 and compares it to an average theoretical longitudinal gauge factor. From Table 5, it can be concluded that the experimental gauge factor for piezoresistor A2 presents an error of around 48% relative to the average theoretical value while piezoresistors B2 presents an error of around 87%. The fact that the maximum gauge factor found is only around 30 times bigger than metal gauge factor values further proves that the hypothesis

that the results obtained are inaccurate, since they do not represent standard gauge factor values for piezoresistive sensors, as previously discussed in section 2.3.

Table 5 - Comparison between experimental longitudinal gauge factor and theoretical longitudinal gauge factor.

Piezoresistor	Experimental Longitudinal Gauge Factor (GF_L)	Theoretical Longitudinal Gauge Factor (GF_L)	Relative Error (%)
A2	67.90	130	47.77
B2	17.41		86.61

To reinforce this conclusion, considering that the variation of strain values of the graphs of Figure 12 is approximately 0.030% for all piezoresistors, we can calculate the resistance change using Equation 9.

$$\frac{\Delta R}{R_0} = 130 \times 3 \times 10^{-4} = 0.039 \quad (15)$$

So, considering the resistance values in Table 2, Table 6 presents the expected range of values considering the resistance change calculated in Equation 15.

Table 6 - Resistance range obtained from the theoretical longitudinal gauge factor from the values in Table 2 for position B.

Resistor	Average Resistance range (kΩ)
A1	[5.27; 5.31]
A2	[5.29; 5.33]
B1	[5.29; 5.33]
B2	[5.25; 5.29]

By analyzing the resistance range presented in Table 6, it is observed that the calculated resistance ranges based on the average gauge factor of silicon deviate significantly from those presented in Figure 11. This deviation reinforces the inconsistency of the obtained results, suggesting that the sensors used may not be behaving as piezoresistive elements. This is further supported by the detailed analysis of Figure 12, where the calculated gauge factor does not align with the theoretical value expected for piezoresistive sensors. In addition to that, relative resistance change analysis indicates significant measurement issues with the piezoresistive sensors, with relative resistance change values having null strain values.

Additionally, analyses performed on positions A, C, and D of the samples revealed similar results to the ones obtained for position B, even though with the approximation made by Equation 15, they are deemed redundant since the strain is considered the same across each sample. However, these additional results are detailed in Annex B and Annex C.

The previous arguments indicate the possibility of systematic errors in the data. Having already ruled out most of the hypotheses related to material failures or measurement methodology errors, the next step is to investigate potential issues in the circuits and the connections between the various electronic components of the measurement system.

4.8 Interface Circuit Testing

First, the samples were tested yet again in the probe setup already shown in Figure 3(a) - section 3.2. This time, instead of having the probe connecting to the sample itself, it was connected to the carrier PCB, after wire bonding to the MEMS samples was completed. The results obtained were like those obtained in Figure 5(a) and Figure 5(b). This demonstrated that the samples are still working correctly and that the wire bond was not an issue as previously theorized.
Next, the same source meter device used for the four-point bending was tested by applying 5V to two through-hole resistors of 4.3 kΩ and 6 kΩ, one at a time. The results obtained are summarized in Table 7. According to Table 7, the problem is not in the source meter since the measurements are accurate when compared to the theoretical values, having a very small relative error of 1.04% for the 4.3 kΩ and 0.26% for the 6 kΩ.

Table 7 - Experimental and theorical comparison of resistance values of a through hole resistor.

Experimental Resistance (kΩ)	Theorical Resistance (kΩ)	Relative error (%)
4.26	4.3	1.04
5.98	6.0	0.26

The next testing made was for the carrier PCB to verify that all connections were made properly when designed. In this testing, a resistor of 4.3k was connected to the pads that are supposed to be wire bonded to the samples. Figure 13(a) represents the setup for the test performed. One of the terminals of the through-hole resistance was connected to a pad meant for one of the piezoresistors' pads and the other terminal was connected to the bulk terminal, according to the wire bond schematic displayed in Figure 9. The carrier PCB was then connected to a multimeter where the positive terminal would coincide with the FPC pad that was meant to connect to a bulk pad, according to the layout of a sensor (See Figure 9), and the negative terminal to a pad on the FPC connector that corresponds to the pad where the other terminal of the resistor is connected. From this test, the resistance measured was around 4.263 kΩ. This test was conducted for all pads, and similar resistance values were measured. With this, it can be concluded that the problem was not the carrier PCB since resistance values correspond to the measured resistor with a very small deviation (~0.86%).

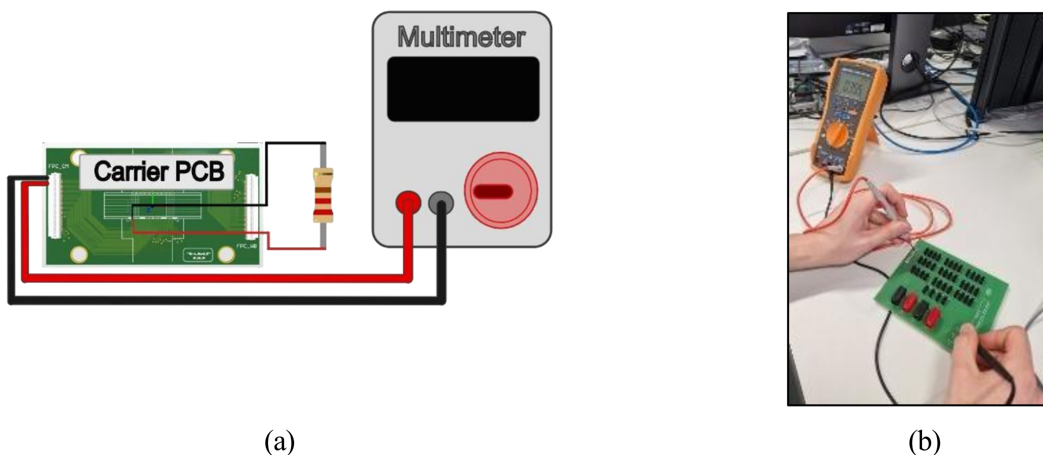

(a) (b)

Figure 13 - Setup used to test: (a) the carrier PCB; (b) the manual switch PCB.

The next set of tests made was for the manual switch PCB to verify that all connections were made properly when designed. In this, a multimeter was used to measure the resistance through the tracks of the PCB. Figure 13(b) represents the setup for the test performed. The first test consisted of measuring resistance by connecting the positive terminal of the multimeter to the pad corresponding to the connection of the bulk layout, according to the wire bonding scheme in Figure 9, and the negative terminal to the output jumper. The second test consisted of measuring resistance by connecting the positive terminal of the multimeter to the input jumper and the negative terminal to the pad corresponding to the connection of the bulk layout, as seen in Figure 9. Both tests presented very low impedance with resistance values around 0.3 Ω.

The next test was made to verify the connection between the carrier PCB and the switch. In this, a resistor of 4.3 kΩ was connected to the pads that are supposed to be wire bonded to the samples, as previously done when analyzing the carrier PCB independently. Figure 14 represents the setup for the test performed. The carrier PCB was then connected to the switch PCB via FPC connection, and the latter was also connected to the source meter via banana connectors. The source meter was set for 5 V. In order to perform the test, the switch corresponding to the terminal should be turned on. All the pads were tested. However, when testing, it was discovered that some resistance values of a few pads were not measuring the intended value. Upon, analyzing carefully the carrier PCB of Figure 8, the wire bonding scheme in Figure 9, and the manual switch PCB of Figure 10 and comparing to the setup used, it was discovered that an error in the design of the switch PCB was made, more precisely in the order of the connections in the FPC connector. For the circuit to work in measuring resistance as intended, the PCB should have inverted the connections on the pins of the FPC in the schematic in Figure 15. In other words, pin 50 of the component "FPC_CM" in the schematic Figure 15 has been pin 1 and vice versa for all 50 pins.

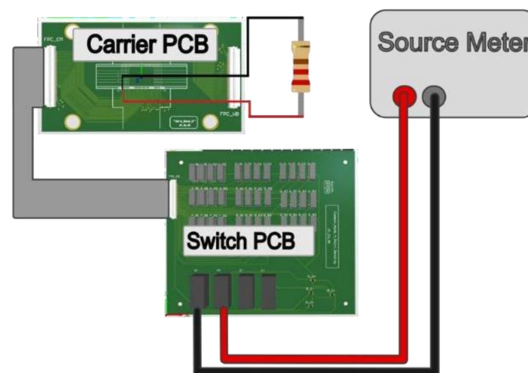

Figure 14 - Setup used to test the carrier PCB and manual switch PCB connection.

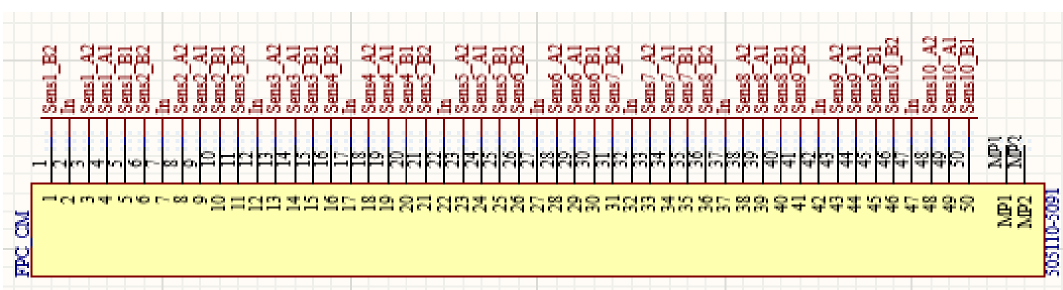

Figure 15 - FPC schematic connections of manual switch PCB (See section 4.5).

Table 8 summarizes the tests conducted and their results. Through the previously conducted tests, it was identified that the issue with the four-point bending resistance measurements stemmed from the manual switch PCB used. The findings in this section further support the conclusions drawn in sections 4.6 and 4.7 and explain the high relative errors observed in the measurements for resistance and the gauge factor. Consequently, it is important to conclude that the analysis does not accurately reflect the actual parameters mentioned earlier, as the obtained values do not align with the expected values for a piezoresistance sensor.

Table 8 - Summary of the tests performed on the PCB's.

Circuitry Test	Functionality
Sample wire bonded	✓
Carrier PCB	✓
Switch PCB	×

4.9 Automatic Interface Circuit PCB

In parallel to the four-point bending measurements and further testing performed to identify the root problem, a second PCB was developed to read resistance values off of the samples more automatically, instead of manual switches. For this purpose, a PCB with an FPC connection to the carrier PCB was developed. Figure 16 shows the layout of the PCB developed. It presents the FPC connection for the carrier PCB, banana connectors for voltage and/or current supply, as well as jumpers to prevent energy spikes from damaging the components and samples.
The main difference from this PCB to the manual switch is in the use of SPST (Single-Pole Single-Throw) switches – the ADGS2414D - instead of manual switches. This method of switching makes use of SPI communication.
SPI Communication is a synchronous serial communication protocol that operates on a master-slave architecture, where the master device controls the communication process. This protocol consists of four primary signals that can be observed in Figure 17. These signals consist of: CLK (Serial Clock) which is generated by the master and synchronizes data transmission between devices; MOSI (Master Out Slave In) which represents the signal through which the master sends data to the slave; MISO (Master In Slave Out) that represents the signal through which the slave sends data back to the master; SS (Slave Select) or CS (Chip Select) is an active-low signal used by the master to select and communicate with a specific slave device [29].

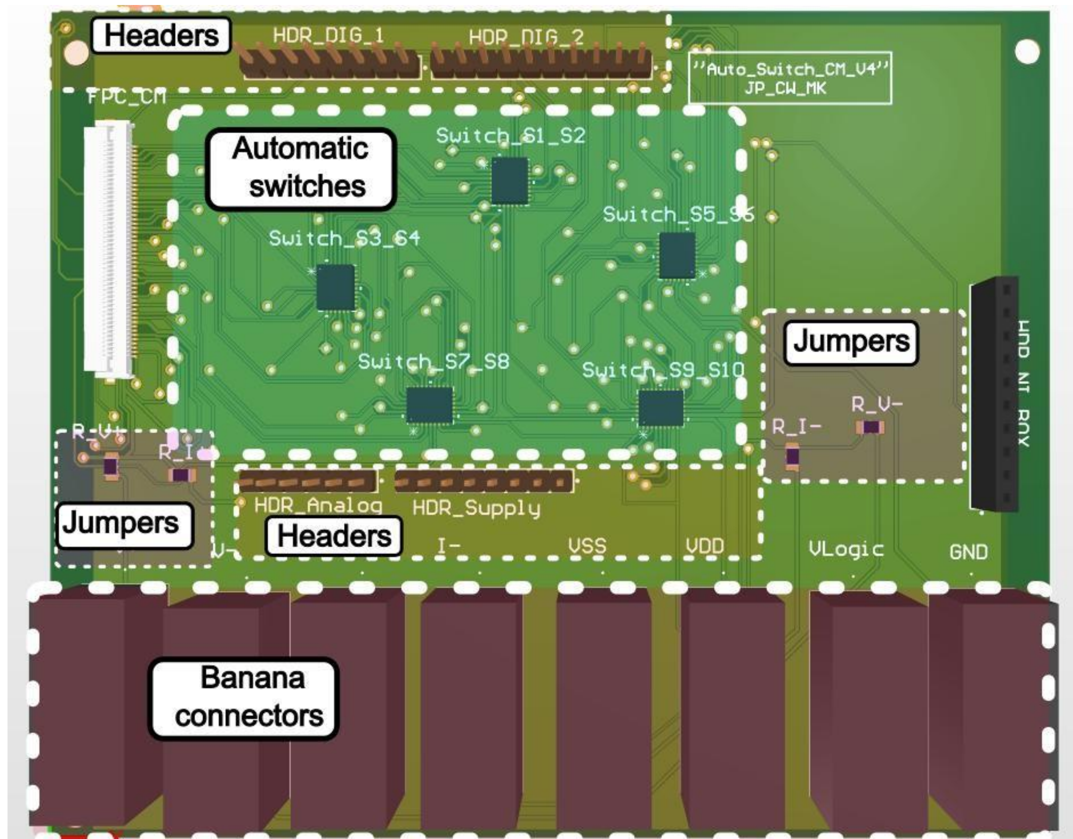

Figure 16 - Top view of the automatic switch PCB.

As seen in Figure 17, when the master intends to communicate with a slave, it pulls the corresponding SS line low, signaling that the slave to become active. The master then generates the CLK signal, and data is simultaneously transmitted from the master to the slave via the MOSI line and from the slave to the master via the MISO line. This exchange continues for the duration of the data frame. Once the data transfer is complete, the master can deselect the slave by setting the SS line high, concluding the communication session.

SPI interfaces have configurable clock polarity (CPOL) and clock phase (CPHA) settings that dictate the timing of data sampling and shifting. The CPOL setting determines the idle state of the clock signal; a CPOL of 0 means the clock idles low, while a CPOL of 1 signifies that it idles high. The CPHA setting indicates which clock edge, either rising or falling, is used for sampling and shifting data. With a CPHA of 0, data is sampled on the leading edge and shifted out on the trailing edge, whereas a CPHA of 1 allows for data to be shifted out on the leading edge while sampling occurs on the trailing edge. Together, CPOL and CPHA result in four possible SPI modes (0 through 3) [30].

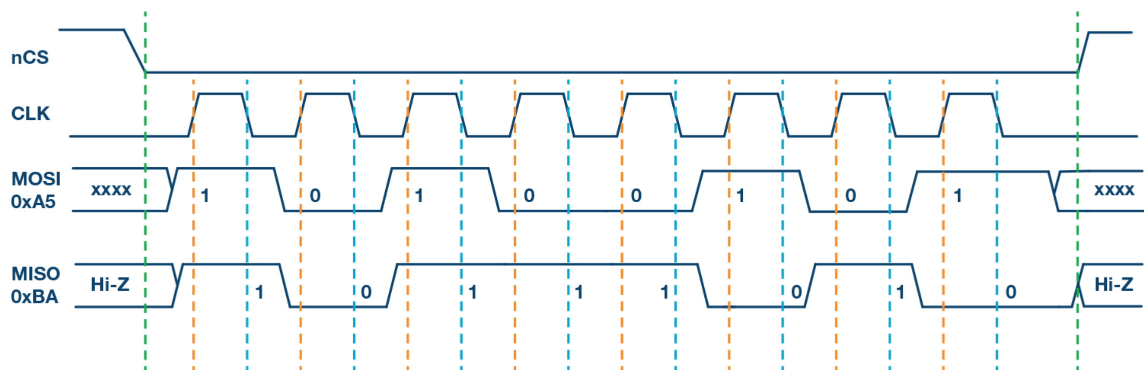

Figure 17 – Example of an SPI Communication Waveform: Data Transfer between Master and Slave (Mode 0) [30].

4.9.1 Implementation

According to the datasheet, the ADGS2414D is a 16-channel switch that operates by accessing its internal registers through address mode, which is the default mode upon power-up. In address mode, each SPI command is structured with a CS falling edge marking the start and a CS rising edge marking the end of the communication cycle. A full SPI frame consists of 16 CLK cycles, where the first bit in the SDI line determines whether a read or write command is issued. If the first bit is set to 0, a write command is executed, whereas if it is set to 1, a read command is initiated. The next seven bits indicate the target register address, while the remaining eight bits either contain the data to be written into the register during a write operation or are used to retrieve data from the register during a read operation. The output data from a read command appears on the SDO line, propagating from the eighth to the fifteenth falling edge of CLK, and a register write occurs on the sixteenth CLK rising edge.

In addition, each ADGS2414D switch requires three voltage inputs to function correctly. As seen in the ADGS2414D datasheet, the VDD pin requires a voltage supply of 12V for single supply, the VSS requires 0 V and the Vlogic pin should align with the logic levels of the controlling microcontroller, with a permissible range of 2.7 V to 5.5 V. This requirement explains the inclusion of various banana connectors on the PCB.

Another important detail in the PCB design is the headers used for connection with an Arduino Uno board, which serves as a master to the five slave devices, the ADGS2414D switches. Each SPI-related pin on the Arduino Uno has a dedicated function based on the Arduino Uno R3 datasheet. The MOSI signal is assigned to digital pin 11, while the MISO signal is connected to digital pin 12. The CLK signal, which synchronizes communication, is provided by digital pin 13. Additionally, the system uses five digital pins, specifically pins 2 through 6, to act as Chip Select lines for the five ADGS2414D switches, allowing the Arduino to control each switch and channel individually.

The PCB is designed to control multiple ADGS2414D switches using SPI communication, allowing users to select which resistor to read at any time. The Arduino Uno is programmed to send 16-bit commands to the ADGS2414D switches. Each switch features 16 channels that users can interact with, and they are controlled by individual chip select (CS) pins, enabling communication with one device at a time.

When users want to interact with a specific switch, they should input commands through a serial interface (in this case, Arduino IDE monitor) to select a device and channel. The Arduino then sends a corresponding SPI command, whose structure was already explained, to the selected switch. The write operation is specifically used to select the channel that corresponds to a specific piezoresistor.

For this setup to work, the Arduino board was programmed with the C++ presented in Annex D.

4.9.2 Testing

In order to verify if the PCB was working correctly, the code presented in Annex D was uploaded onto the Arduino Uno board and connected to a computer to test the user inputs. Meanwhile, digital pins 2,3,4,5,6,11,12 and 13 were observed in pairs in an oscilloscope.

The timing diagram of Figure 18 represents some of the tests made by sending commands, previously explained in section 4.9.1, from the Arduino with a clock (CLK) of 1 MHz.

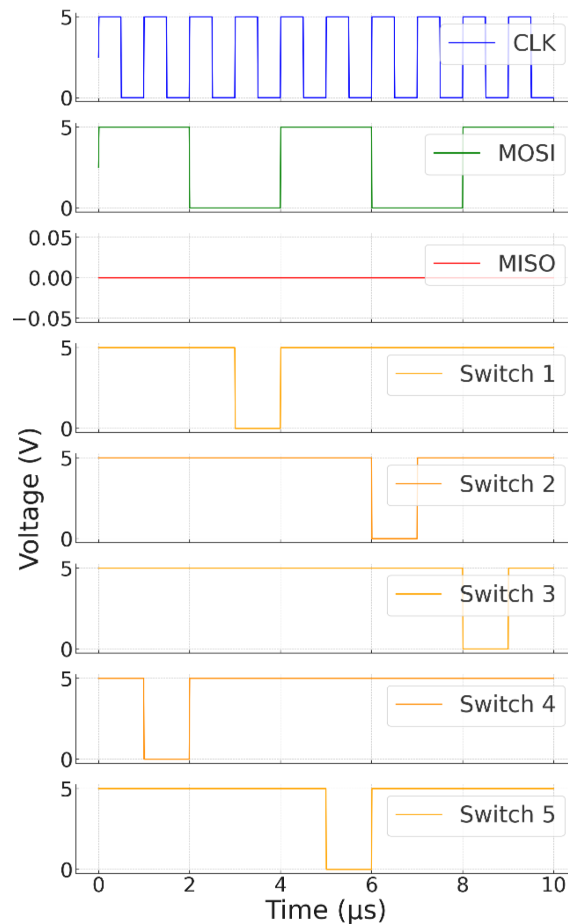

Figure 18 - Timing diagram of the signals from digital pins 2,3,4,5,6,11,12 and 13 from Arduino Uno board.

The results obtained confirm that the master sends out signals. However, since no slave devices were connected, there is no response from the MISO signal. Since the switches have a particular command structure, they were tested with the carrier PCB directly.

With the setup observed in Figure 19, resistance was read by applying 5V for VDD and V+, 3.3V for VLogic, and 0V for VSS and GND connectors. The resistance values read from the source meter presented values in the MΩ scale, with many instabilities in the readings when sending SPI commands.

Upon careful analysis of the schematics in Figure 15 and Figure 20, it was concluded that a design error occurred in the automatic switch PCB, particularly in the order of the connections within the FPC connector, similar to the manual switch PCB. For the circuit to accurately measure resistance as intended, the connections on the pins of the FPC in the schematic from Figure 20 needed to be reversed in order. Specifically, pin 50 of the component "FPC_CM" should have been designated as pin 1, and this inversion should apply to all 50

pins. Consequently, this design oversight was identified as the source of the issue, confirming that the original problem was not with the SPI functioning but rather with the incorrect layout of the automated switch PCB.

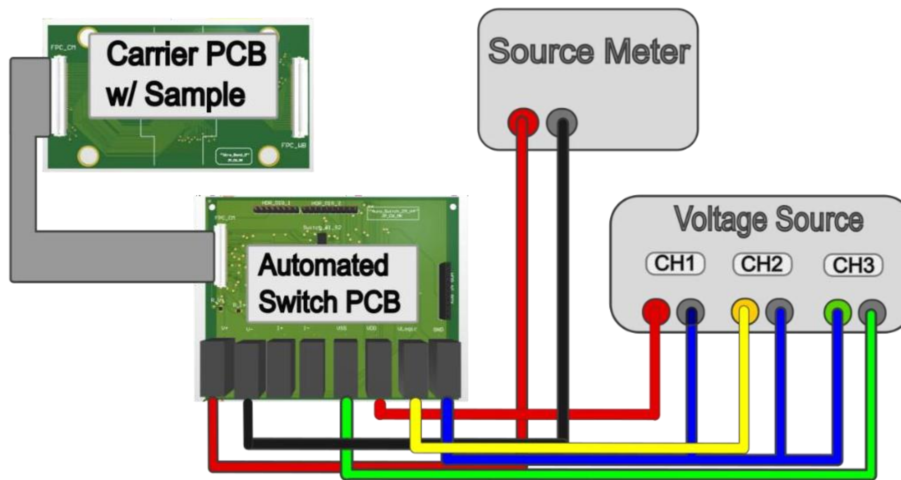

Figure 19 - Setup used to test the automatic switch PCB directly with the samples.

FPC_CM?

Pin	Net
1	Sens1_B2
2	In
3	Sens1_A2
4	Sens1_A1
5	Sens1_B1
6	Sens2_B2
7	In
8	Sens2_A2
9	Sens2_A1
10	Sens2_B1
11	Sens3_B2
12	In
13	Sens3_A2
14	Sens3_A1
15	Sens3_B1
16	Sens4_B2
17	In
18	Sens4_A2
19	Sens4_A1
20	Sens4_B1
21	Sens5_B2
22	In
23	Sens5_A2
24	Sens5_A1
25	Sens5_B1
26	Sens6_B2
27	In
28	Sens6_A2
29	Sens6_A1
30	Sens6_B1
31	Sens7_B2
32	In
33	Sens7_A2
34	Sens7_A1
35	Sens7_B1
36	Sens8_B2
37	In
38	Sens8_A2
39	Sens8_A1
40	Sens8_B1
41	Sens9_B2
42	In
43	Sens9_A2
44	Sens9_A1
45	Sens9_B1
46	Sens10_B2
47	In
48	Sens10_A2
49	Sens10_A1
50	Sens10_B1
MP1	MP1
MP2	MP2

505110-5091

Figure 20 - Schematic of the automatic switch PCB.

5 CONCLUSION AND FUTURE PROSPECTS

This study provides a comprehensive characterization of MEMS pressure sensors based on the piezoresistive effect, with a specific focus on the common node configuration employed in the analyzed samples. Each sensor incorporated four piezoresistive pads (A1, A2, B1, and B2), and four designated sensing positions (A, B, C, and D) were available within each sample.
The initial current-voltage (I-V) characterization, conducted without any mechanical stress, established baseline resistance values that exhibited the expected linear behavior. With high correlation coefficients ($R^2 > 0.999$), these results validated the resistance measurements obtained under static conditions. However, considerable discrepancies arose when comparing the baseline resistance values to those determined during the four-point bending tests. The deviations reached relative errors as high as 16.8%, indicating systematic errors within the measurement setup that needed further investigation.
An analysis of the relative resistance change in response to applied strain revealed anomalous behavior among several sensors, as they demonstrated resistance variations in the absence of applied strain, which contradicts the concept of piezoresistivity. The gauge factor analysis corroborated these findings, revealing values below 100 across all measured samples. This is notably lower than the expected range for silicon piezoresistors (typically 130 to 200). Published results as low as 17 suggest significant issues with measurement accuracy and reliability, leading to the conclusion that the data collected cannot be deemed a valid representation of the true piezoresistive response of these sensors.
In addressing the root causes of these inconsistencies, a thorough assessment of all components within the measurement circuitry was conducted. While the source meter and carrier PCB functioned as intended, design flaws in both the manual and automatic switch PCBs, specifically related to the reversed pinout configuration of the FPC connectors, resulted in misrouted connections to the sample that were wire bonded and inaccurate data acquisition. Even though SPI communication was effectively implemented in the automatic switch via an Arduino-controlled architecture, the same design flaw replicated the issues experienced in the manual switch system.
Looking ahead, several enhancements are needed for achieving reliable characterization of MEMS piezoresistive sensors. First, among these is the redesign of the switch and automatic switch PCBs to correct FPC pin mapping. This correction should be followed by comprehensive four-point bending testing to evaluate the sensor's piezoresistive behaviour. Following this, more analysis should be done to evaluate the physical positioning relative to the applied stress region, potentially varying the distances between inner and outer supports of the four-point bending setup to systematically investigate stress distribution effects. Moreover, expanding the number of sensors analyzed per sample beyond the initial four will increase the statistical significance of the findings and broaden the coverage of the results.
Furthermore, the experimental setup warrants upgrades. The integration of the automatic switch system with a LabVIEW-controlled environment would facilitate full automation of channel selection, enhancing repeatability, efficiency, and control in the measurement process. Additionally, subsequent testing, particularly focused on temperature-dependent characterization, is essential to evaluate the thermal effects on sensor behavior, which were not considered in the current study.
In conclusion, the systematic errors identified in the switching circuitry and limitations in the mechanical setup significantly hindered the ability to extract valid performance metrics under stress. By implementing the corrections and improvements outlined in this thesis, future research endeavors will be better positioned to provide

accurate and comprehensive evaluations of the behavior of piezoresistive MEMS sensors, ultimately contributing to the advancement of this technology in practical applications.

6 BIBLIOGRAPHY

[1] N. Hossain *et al.*, “Advances of materials science in MEMS applications: A review,” Jun. 01, 2024, *Elsevier B.V.* doi: 10.1016/j.rineng.2024.102115.

[2] S. Finkbeiner, “MEMS for automotive and consumer electronics,” Sep. 2013, doi: https://doi.org/10.1109/essderc.2013.6818809.

[3] Persistence Market Research, “MEMS Pressure Sensors Market Poised for Significant Growth, Projected to Reach US$9.5 Billion by 2030, Persistence Market Research Predicts.” Accessed: Oct. 23, 2024. [Online]. Available: https://www.globenewswire.com/news-release/2024/01/11/2808271/0/en/MEMS-Pressure-Sensors-Market-Poised-for-Significant-Growth-Projected-to-Reach-US-9-5-Billion-by-2030-Persistence-Market-Research-Predicts.html

[4] A. DeHennis, J. Chae, and A. Baroutaji, “Comprehensive Microsystems,” in *Reference Module in Materials Science and Materials Engineering*, Elsevier, 2008, ch. Pressure Sensors. doi: 10.1016/B978-0-12-803581-8.00541-5.

[5] Kovacs G, “Micromachined Transducers Sourcebook,” McGraw-Hill Science/Engineering/Math, 1998, pp. 210–215.

[6] A. S. Fiorillo, C. D. Critello, and A. S. Pullano, “Theory, technology and applications of piezoresistive sensors: A review,” Oct. 01, 2018, *Elsevier B.V.* doi: 10.1016/j.sna.2018.07.006.

[7] K. B. Balavalad, S. Meti, K. B. Balavald, and B. G. Sheeparmatti, “MEMS Piezoresistive Pressure Sensor: A Survey,” 2016. [Online]. Available: www.ijera.com

[8] S. S. Kumar and B. D. Pant, “Design principles and considerations for the ‘ideal’ silicon piezoresistive pressure sensor: A focused review,” *Microsystem Technologies*, vol. 20, no. 7, pp. 1213–1247, 2014, doi: 10.1007/s00542-014-2215-7.

[9] Y. Sun, S. E. Thompson, and T. Nishida, *Strain effect in semiconductors: Theory and device applications*. Springer US, 2010. doi: 10.1007/978-1-4419-0552-9.

[10] C. S. Smith, “Piezoresistance Effect in Germanium and Silicon,” Physical Review, vol. 94, no. 1, pp. 42–49, Apr. 1954, doi: https://doi.org/10.1103/physrev.94.42.

[11] M. Bao, “Analysis and Design Principles of MEMS Devices,” 1st ed., Elsevier Science, 2005, pp. 1–261.

[12] Gardner J, Varadan V, and Awadelkarim O, *Microsensors, MEMS, and Smart Devices*. John Wiley & Sons, Ltd,., 2001. doi: 10.1002/9780470846087.

[13] K. N. Bhat, “Silicon Micromachined Pressure Sensors,” *Journal of the Indian Institute of Science*, vol. 87, 2007.

[14] B. Maes, A. Wiel, and J. Vergauwen, “Pressure sensor resistor configuration for stress compensation,” US 20240288325A1, Aug. 29, 2024

[15] Y. Zhang *et al.*, “Investigation of potting-adhesive-induced thermal stress in mems pressure sensor,” *Sensors*, vol. 21, no. 6, pp. 1–11, Mar. 2021, doi: 10.3390/s21062011.

[16] J. Zeng, X. Chen, X. Du, and Q. Zhu, “Research on temperature compensation of MEMS pressure sensors based on optimized multi-kernel relevance vector machine,” in *Journal of Physics: Conference Series*, Institute of Physics, 2024. doi: 10.1088/1742-6596/2897/1/012052.

[17] C. Wohlgemuth, A. Leidl, G. Feiertag, and W. Pahl, “P1.14 - Miniaturised Ceramic Packages for Piezoresistive Pressure Sensors,” Proceedings SENSOR 2009, Volume II, pp. 295–300, 2009, doi: https://doi.org/10.5162/sensor09/v2/p1.14.

[18] M. Zhang, L. Du, Z. Zhao, and Z. Fang, “Low-stress packaging for a MEMS atmosphere pressure sensor,” Apr. 2013, doi: https://doi.org/10.1109/nems.2013.6559817.

[19] S. H. Choa, M. C. Lee, and Y. C. Cho, “Effects of Packaging Induced Stress on MEMS Devices and Its Improvements,” *Key Eng Mater*, vol. 326–328, pp. 529–532, Dec. 2006, doi: 10.4028/www.scientific.net/kem.326-328.529.

[20] X. Han *et al.*, “Advances in high-performance MEMS pressure sensors: design, fabrication, and packaging,” Dec. 01, 2023, *Springer Nature*. doi: 10.1038/s41378-023-00620-1.

[21] X. Dong, H. Zhao, L. Zhang, H. Cheng, and J. Gao, “Geometry effects in four-point bending test for thin sheet studied by finite element simulation,” *Mater Trans*, vol. 57, no. 3, pp. 335–343, 2016, doi: 10.2320/matertrans.M2015178.

[22] C. J. Wilson and P. A. Beck, “Fracture Testing of Bulk Silicon Microcantilever Beams Subjected to a side load,” *Journal of Microelectromechanical Systems*, vol. 5, no. 3, pp. 142–150, Sep. 1996, doi: https://doi.org/10.1109/84.536620.

[23] S. Nakao, T. Ando, M. Shikida, and K. Sato, “Tensile test of single crystal silicon film at elevated temperatures,” Micro-Nanomechatronics and Human Science, 2004 and The Fourth Symposium Micro-Nanomechatronics for Information-Based Society, 2004., pp. 1–5, doi: https://doi.org/10.1109/mhs.2004.1421278.S. Timoshenko and J. Goodier, *Theory of Elasticity*, 2nd ed. McGraw-Hill Book Company, 1951.

[24] O. A. Bauchau, “A beam theory for anisotropic materials,” *Journal of Applied Mechanics, Transactions ASME*, vol. 52, no. 2, pp. 416–422, 1985, doi: 10.1115/1.3169063.

[25] D. Young, K. Johnson, S. Stadler, and J. Cutnell, *Physics, 10th Edition*, p. 544, 2014.

[26] T. Yi, L. Li, and C.-J. Kim, “Microscale material testing of single crystalline silicon: process effects on surface morphology and tensile strength,” 2000. [Online]. Available: www.elsevier.nlrlocatersna

[27] W. A. Brantley, “Calculated elastic constants for stress problems associated with semiconductor devices,” *J Appl Phys*, vol. 44, no. 1, pp. 534–535, 1973, doi: 10.1063/1.1661935.

[28] J. W. . Valvano, “Embedded systems. Volume 1, Introduction to the ARM® Cortex(TM)-M3 microcontrollers,” Jonathan W. Valvano, 2019, ch. 9.6, pp. 401–417.

[29] P. Dhaker and A. Devices, “Clock Polarity and Clock Phase,” Sep. 2018. [Online]. Available: https://www.analog.com/en/resources/analog-dialogue/articles/introduction-to-spi-interface.html

7 ANNEX A - 3D PIECE DESIGN

For the four-point bending setup, 3D-printed pieces were utilized as inner and outer supports. Figure 21 shows the design of the piece used as the inner support, which features a 10 mm contact distance. This piece was consistently secured with a screw at the bottom of the four-point bending setup.
The design of the outer support piece posed a more complex challenge. The initial design, shown in Figure 22(a), frequently caused wire breakage in the samples because the piece tended to shift sideways when removed from the setup. As a solution, it was redesigned to include holes that could slide over the beams of the setup, as depicted in Figure 22(b).

Figure 21 - 3D piece used for inner support on the four-point bending setup.

(a)

(b)

Figure 22 - (a) old design of 3D Piece for outer support; (b) new design for 3D piece for outer support.

Although they were not used in this particular work, several other designs were created with larger contact distances in order to test different contact points, with the example of a 30 mm contact distance presented in Figure 23.

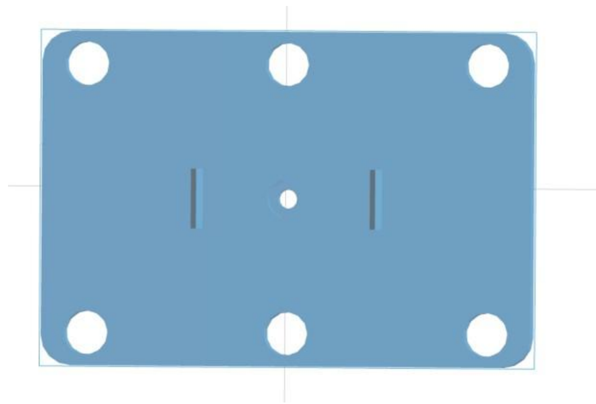

Figure 23 - 3D piece design for outer support of the four-point bending setup with 30 mm contact distance

8 ANNEX B - RESISTANCE ANALYSIS

As previously explained the samples used in the four-point bending test were analyzed in four different positions (See Figure 6). In similarity to what was done for position B, the resistance will be analyzed in this section for positions A, C, and D.
For positions A, C and D, the resistance, in kΩ, in function of stress, in MPa, can be observed for the four piezoresistors of the sensor in Figure 24, Figure 25 and Figure 26.

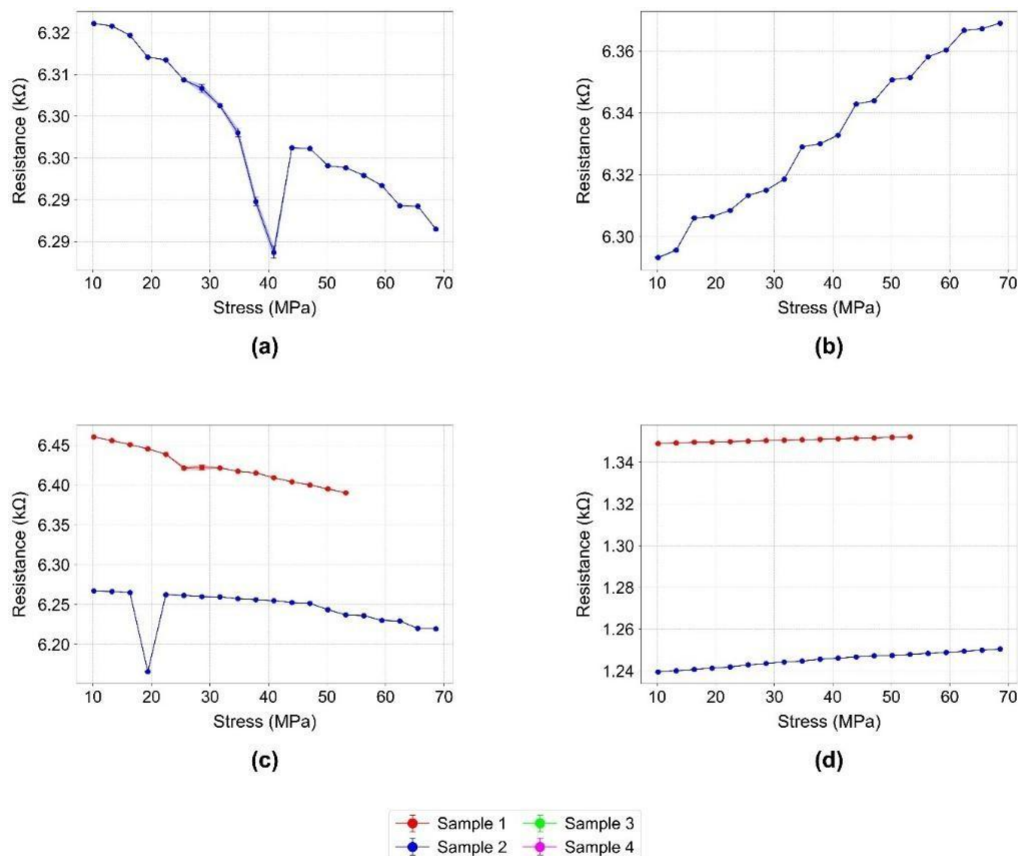

Figure 24 – Resistance (kΩ) in function of stress (MPa) across position A in sample 1, sample 2 for: (a) piezoresistor A1, (b) piezoresistor A2, (c) piezoresistor B1, (d) piezoresistor B2.

For Position A, it is possible to observe a similar trend with what happen in position B. In Figure 24(a) Piezoresistor A1, more precisely, sample goes from 6.32 kΩ to 6.29 kΩ, with a big fluctuation in stress region from 30 MPa to 50 MPa. In Figure 24(b), sample demonstrates a steady increase around the 6.30 kΩ to 6.37 kΩ for piezoresistor A2. Figure 24(c) demonstrates that piezoresistor B1 shows a less steady decrease in resistance for both samples 1 and sample 2 when compared to piezoresistor A1. The same

is seen in Figure 24(d) where the resistance increase for piezoresistor B2 is way less steady than that of piezoresistor A2 varying from 1.24 kΩ to 1.25 kΩ.
Figure 25 shows position C with similar results to the two previous positions. For piezoresistor A1, in Figure 25(a) resistance decreases from approximately an average of 6.40 kΩ to 6.30 kΩ for samples 1 and 3. Sample 2 presents similar behaviour except it has a fluctuation at lower stress of around 10 MPa. Figure 25(b) presents a less linear relationship with an increase of sample 2 resistance from 6.57 kΩ to 6.63 kΩ for piezoresistor A2. Piezoresistor B1 presents a more linear behaviour, as shown in Figure 25(c), with samples decreasing from around 6.50 kΩ to around 6.40 kΩ.
At last, in Figure 25(d), sample 3 presents a variation from 1.435 kΩ to 1.44kΩ while sample 2 suffers fluctuations varying between 1.42 kΩ to 1.48 kΩ.

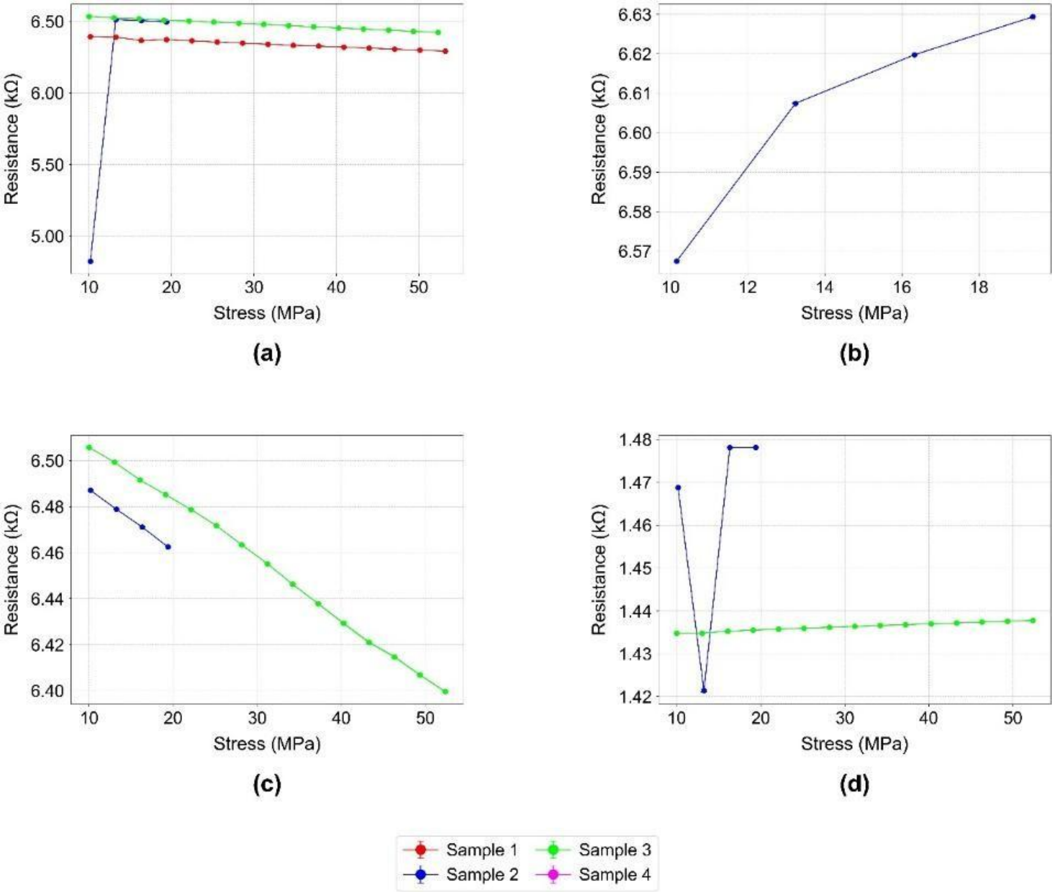

Figure 25 –Resistance (kΩ) in function of stress (MPa) across position C in sample 1, sample 2 for: (a) piezoresistor A1, (b) piezoresistor A2, (c) piezoresistor B1, (d) piezoresistor B2.

In Figure 26, position D was only analyzed for sample 4 due to wire bonding breakage. For piezoresistor A1 show in Figure 26(a), shows a linear variation of resistance from 6.18 kΩ to 6.14 kΩ. Piezoresistor A2 presents big fluctuations in a lower stress range with overall resistance varying little from the 6 kΩ value, as seen in Figure 26(b).

Figure 26(c) presents a linear decrease of resistance, like expected of a transversal piezoresistor, having around 6.41 kΩ in the end.
Figure 26(d) shows piezoresistor B2 with big fluctuations, seemingly increasing resistance from 1.39 kΩ to 1.40 kΩ.

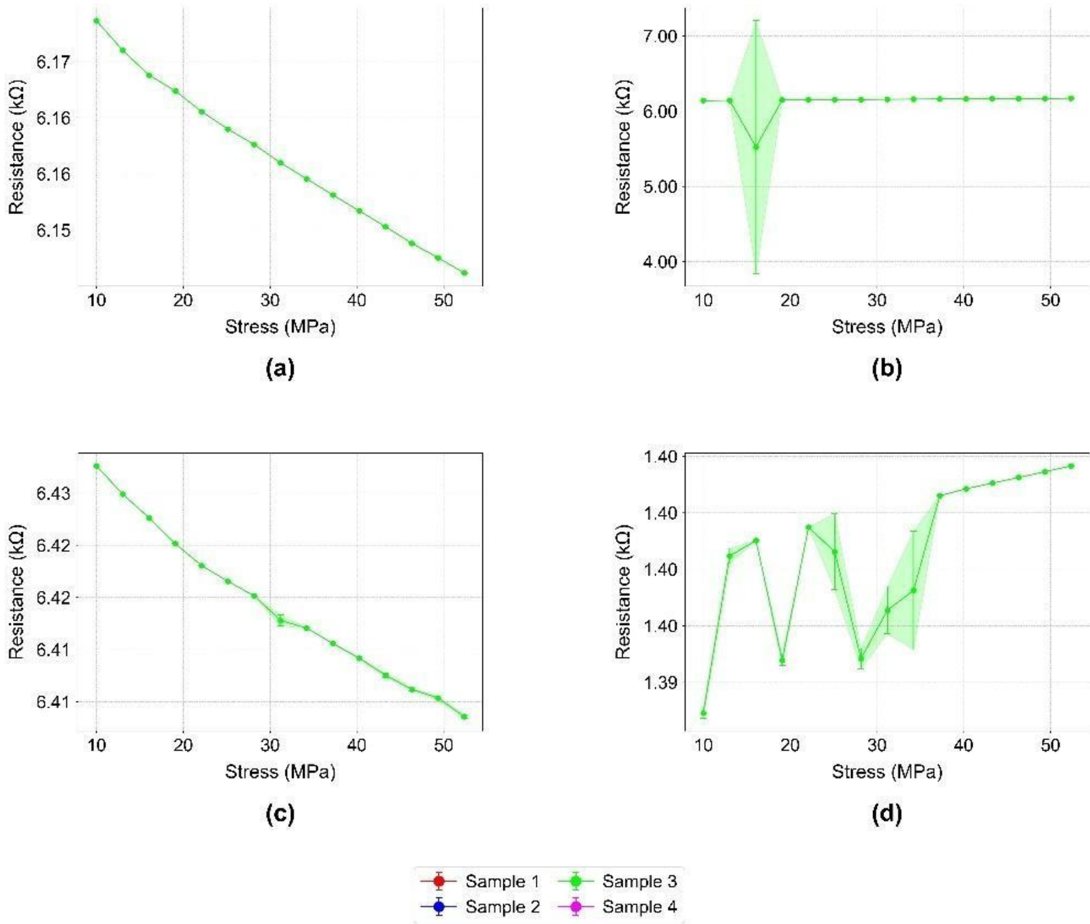

Figure 26 –Resistance (kΩ) in function of stress (MPa) across position D in sample 1, sample 2 for: (a) piezoresistor A1, (b) piezoresistor A2, (c) piezoresistor B1, (d) piezoresistor B2.

The results observed in Figure 24, Figure 25 and Figure 26, for positions A, C and D are consistent with the ones already analyzed for position B, as seen in Table 4, due to the approximation made with Equation 15. These results present resistance values in the range of 6 kΩ which deviates a lot from the resistance values obtained in section 4.2. They also confirm that the orientation of the piezoresistors in the sensor is important due to the slope of curves. Additionally, these values present once again high relative errors, as already observed in Position B, more precisely in Table 2 for similar resistance values.
Therefore, it can be concluded that the results obtained in this section for positions A, C, and D are very similar to the results obtained in section 4.6 for position B.

9 | Annex C - Gauge Factor analysis

The gauge factor was analyzed for positions A, C, and D, similar to the analysis conducted for position B. Relative resistance change serves as a normalization of the resistance change. Since resistance values were previously examined in Annex B, Figure 24, Figure 25, and Figure 26 will not be reanalyzed.
As noted for position B, positions A, C, and D also contain samples that exhibit a change in resistance even when no strain is applied. For instance, sample 2 in position A and sample 1 in piezoresistor A1 of position C demonstrate this behavior. While not every position shows this exact anomaly, certain samples, such as sample 1 in piezoresistor B1 of position A, display trends of resistance change without applied strain. This phenomenon is anomalous because, according to Equation 8, the piezoresistive effect should not occur without strain.

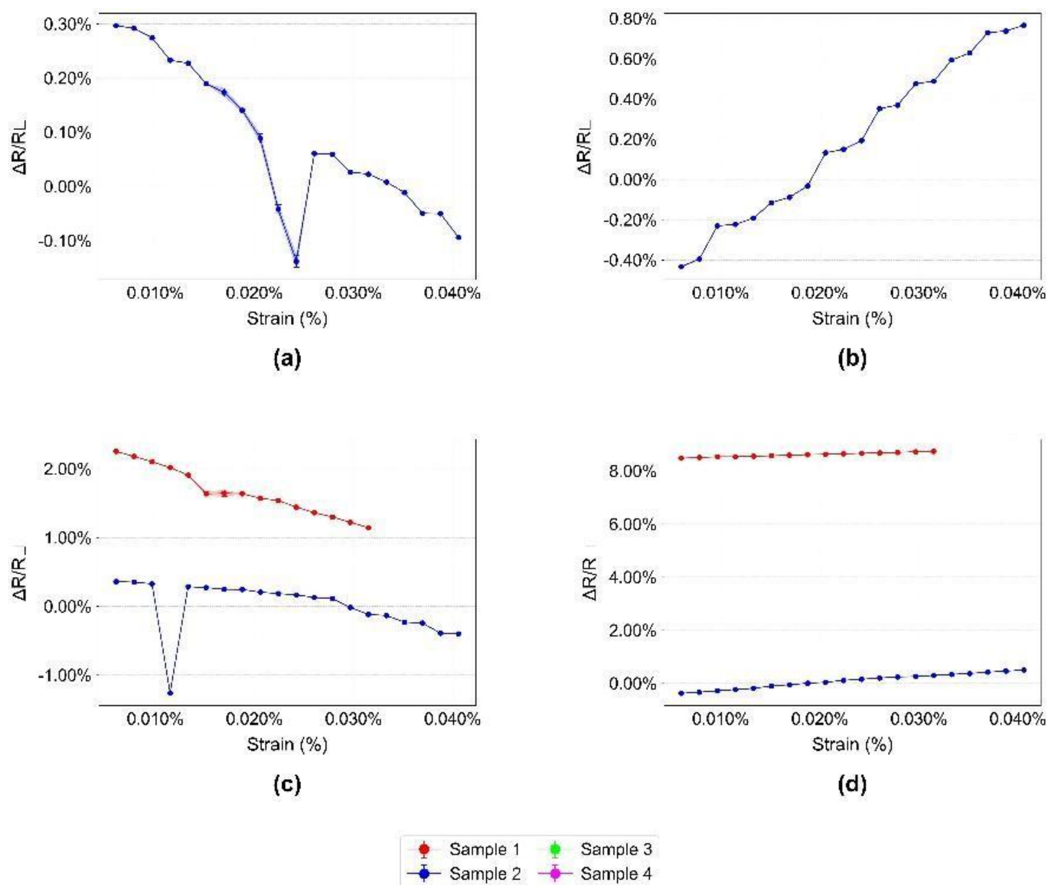

Figure 27 - Relative resistance change in function of strain (%) across position A for sample 1, sample 2, sample 3 and sample 4 for: (a) piezoresistor A1, (b) piezoresistor A2, (c) piezoresistor B1, (d) piezoresistor B2.

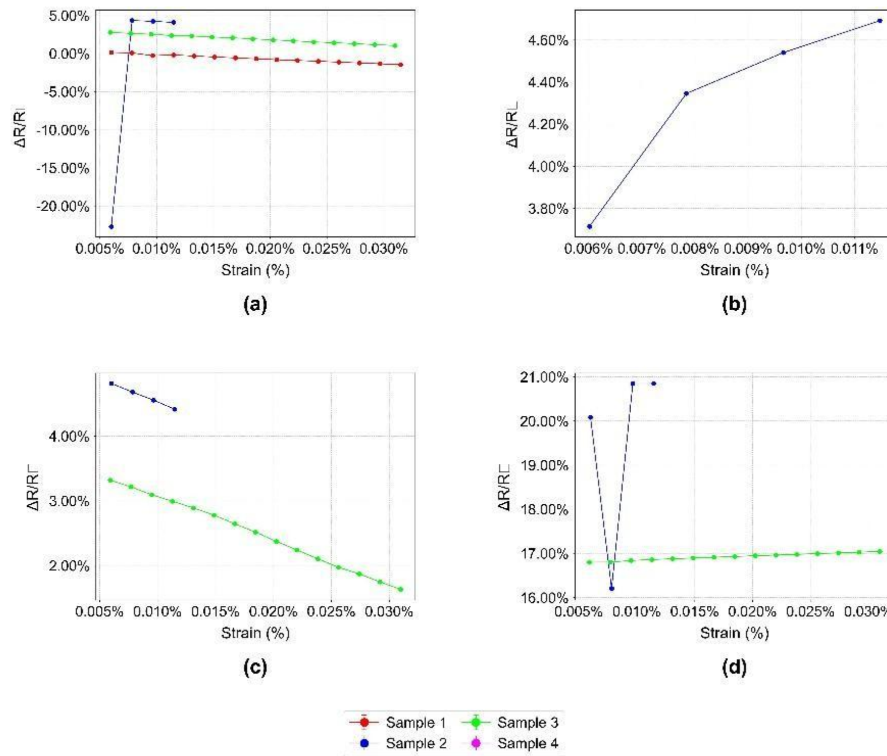

Figure 28 - Relative resistance change in function of strain (%) across position C for sample 1, sample 2, sample 3 and sample 4 for: (a) piezoresistor A1, (b) piezoresistor A2, (c) piezoresistor B1, (d) piezoresistor B2.

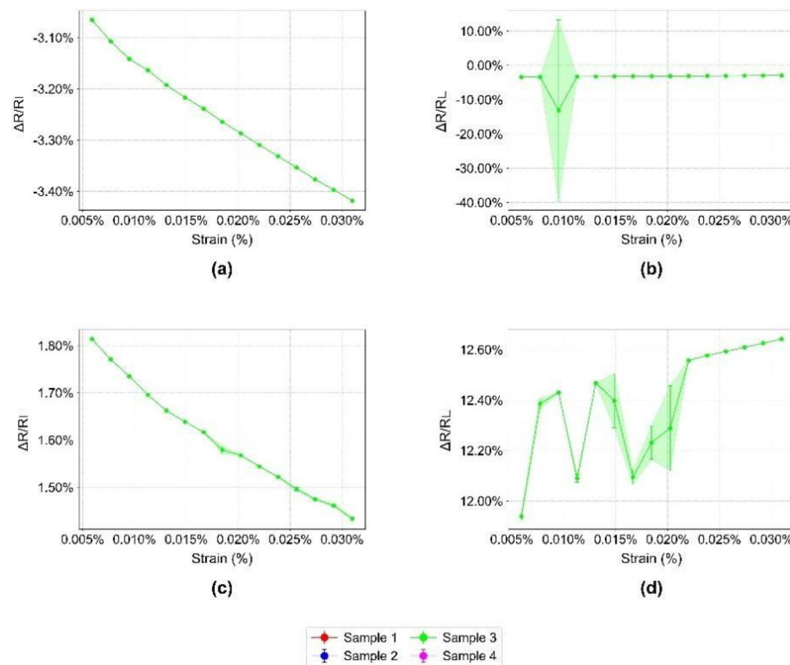

Figure 29 - Relative resistance change in function of strain (%) across position D for sample 1, sample 2, sample 3 and sample 4 for: (a) piezoresistor A1, (b) piezoresistor A2, (c) piezoresistor B1, (d) piezoresistor B2.

As previously done for position B, the longitudinal gauge factor was also determined for positions A, C and D. The same theoretical value for the longitudinal gauge factor is considered. Once again, the slope of each graph of relative resistance change vs stress is the gauge factor of each piezoresistor,

Table 9 presents the comparison of each average gauge factor across samples for longitudinal piezoresistors A2 and B2 of positions A, C and D and compares it to an average theoretical longitudinal gauge factor.

From Table 9, it can be concluded that the experimental gauge factors found are not accurate since they have errors between 35% and 95%, with piezoresistor B2 of position C presenting gauge factor similar to that of metals. In contrast, piezoresistor A2 presents a very good gauge factor since the silicon gauge factor can go up to 200. However, the rest of the values are at most 40 times bigger than that of metals therefore, the existence of a piezoresistive effect comparable to that of silicon is disregarded. This is strengthened by the lack of precision in the results obtained.

In conclusion, the results obtained for positions A, C, and D are very similar to those found for position B in section 4.7. This is still due to the fact that an approximation was made with Equation 15 resulting in considering an uniform strain across each sample.

Table 9 - Comparison between experimental longitudinal gauge factor and theoretical longitudinal gauge factor for positions A, C and D.

Position	Piezoresistor	Experimental Longitudinal Gauge Factor (GF_L)	Theoretical Longitudinal Gauge Factor (GF_L)	Relative Error (%)
A	A2	36.2	130	72.15
	B2	17.37		86.63
C	A2	83.6		35.69
	B2	5.41		95.84
D	A2	198		52.31
	B2	19.6		84.92

10 ANNEX D - ARDUINO CODE

```
1  #include <SPI.h>
2
3  // Define SPI settings
4  const int numDevices = 5;
5  const int chipSelectPins[numDevices] = {2, 3, 4, 5, 6};  // CS pins for each ADGS2414
6  const int numChannels = 8;      // Number of channels
7
8  // Initialize SPI settings
9  SPISettings spiSettings(1000000, MSBFIRST, SPI_MODE0);
10
11 // Data arrays to simulate channel states
12 uint16_t channelStates[numDevices][numChannels];  // Array to store simulated channel states
13
14 void setup() {
15   Serial.begin(9600);
16   SPI.begin();  // Initialize SPI
17
18   // Configure the CS pins as output and set them high
19   for (int i = 0; i < numDevices; i++) {
20     pinMode(chipSelectPins[i],  OUTPUT);
21     digitalWrite(chipSelectPins[i],  HIGH);
22   }
23
24   // Initialize random seed with millis()
25   randomSeed(millis());
26
27   // Initialize channel states to some default values
28   for (int i = 0; i < numDevices; i++) {
29     for (int j = 0; j < numChannels; j++) {
30       channelStates[i][j] = 0xFFFF;  // Initialize with default value
31     }
32   }
33 }
34
35 void loop() {
36   if (Serial.available() > 0) {
```

```
37    String input = Serial.readStringUntil('\n');
38    input.trim();  // Remove any leading/trailing whitespace
39
40    int delimiterIndex = input.indexOf(';');
41    if (delimiterIndex == -1) {
42      Serial.println("Invalid input format. Use 'device_number;channel_number'.");
43      return;
44    }
45
46    int deviceNumber = input.substring(0, delimiterIndex).toInt();
47    int channelNumber = input.substring(delimiterIndex + 1).toInt();
48
49    if (deviceNumber < 1 || deviceNumber > numDevices || channelNumber < 1 || channelNumber >
numChannels) {
50      Serial.println("Invalid device or channel number.");
51      return;
52    }
53
54    // Generate random data for the specified channel
55    uint16_t dataToSend = random(0xFFFF);  // Generate random data
56
57    // Send data to the specified channel
58    sendDataToChannel(deviceNumber - 1, channelNumber, dataToSend);
59
60    // Update the simulated channel state
61    channelStates[deviceNumber - 1][channelNumber - 1] = dataToSend;
62
63    // Simulate reading the data
64    uint16_t dataRead = channelStates[deviceNumber - 1][channelNumber - 1];
65
66    // Print the data sent and the simulated data read
67    Serial.print("Data sent to Device ");
68    Serial.print(deviceNumber);
69    Serial.print(", Channel ");
70    Serial.print(channelNumber);
71    Serial.print(": 0x");
72    Serial.println(dataToSend, HEX);
73
74    Serial.print("Data read from Device ");
75    Serial.print(deviceNumber);
76    Serial.print(", Channel ");
77    Serial.print(channelNumber);
```

```
78     Serial.print(": 0x");
79     Serial.println(dataRead, HEX);
80   }
81 }
82
83 void sendDataToChannel(int deviceIndex, int channel, uint16_t data) {
84   SPI.beginTransaction(spiSettings);
85   digitalWrite(chipSelectPins[deviceIndex], LOW);
86
87   // Send address command to select the shift register
88   SPI.transfer16(0x01); // Address command to select the shift register
89
90   // Prepare data to control channels
91   uint16_t channelData = 0;
92   for (int i = 0; i < numChannels; i++) {
93     if (i == (channel - 1)) {
94       channelData |= (data & 0x01) << i; // Set or clear bit based on data
95     } else {
96       channelData |= (channelStates[deviceIndex][i] & 0x01) << i; // Maintain current state
97     }
98   }
99
100   // Send the data to configure the channels
101   SPI.transfer16(channelData);
102
103   digitalWrite(chipSelectPins[deviceIndex], HIGH);
104   SPI.endTransaction();
105 }
```

2025 JOÃO PIÇARRA Characterization of MEMS Piezoresistive Pressure Sensors

NOVA
NOVA SCHOOL OF
SCIENCE & TECHNOLOGY